CANCER

Cancer mutations rewire the RNA methylation specificity of METTL3-METTL14

Chi Zhang[1], Robyn L. Scott[1], Luiza Tunes[1], Meng-Hsiung Hsieh[2], Ping Wang[1], Ashwani Kumar[3], Brijesh B. Khadgi[1], Yen-Yu Yang[4], Katelyn A. Doxtader Lacy[1], Emily Herrell[1], Xunzhi Zhang[3], Bret Evers[5], Yinsheng Wang[4], Chao Xing[3], Hao Zhu[2], Yunsun Nam[1]*

Chemical modification of RNAs is important for posttranscriptional gene regulation. The METTL3-METTL14 complex generates most *N*^{6}-methyladenosine (m^{6}A) modifications in messenger RNAs (mRNAs), and dysregulated methyltransferase expression has been linked to cancers. Here we show that a changed sequence context for m^{6}A can promote oncogenesis. A gain-of-function missense mutation from patients with cancer, METTL14^{R298P}, increases malignant cell growth in culture and transgenic mice without increasing global m^{6}A levels in mRNAs. The mutant methyltransferase preferentially modifies noncanonical sites containing a GGAU motif, in vitro and in vivo. The m^{6}A in GGAU context is detected by the YTH family of readers similarly to the canonical sites but is demethylated less efficiently by an eraser, ALKBH5. Combining the biochemical and structural data, we provide a model for how the cognate RNA sequences are selected for methylation by METTL3-METTL14. Our work highlights that sequence-specific m^{6}A deposition is important and that increased GGAU methylation can promote oncogenesis.

INTRODUCTION

Specific and controlled modification of mRNAs with N^6-methyladenosine (m^{6}A) is essential for proper gene expression (*1*, *2*). METTL3 and METTL14 form a heterodimeric methyltransferase responsible for most m^{6}A modifications in mRNAs (*3*–*5*). Dysregulated expression of METTL3 or METTL14 affects mRNA m^{6}A modification levels (*3*, *6*). Several cancers have been linked to METTL3-METTL14 overexpression and increased global m^{6}A levels in mRNAs, but the molecular mechanism is complex and context dependent (*7*–*9*). Transcriptome-wide mapping of m^{6}A sites affected by METTL3-METTL14 has shown that the preferred RNA targets of METTL3-METTL14 contain the motif DRACH (D, G/A/U; R, G/A; H, A/U/C), with a dominant Cyt following the methylated Ade (*10*–*13*). However, how the major m^{6}A writer complex recognizes the preferred target RNA sequence is still not understood. Furthermore, the biological and molecular consequence of changing the substrate preference is yet unknown.

In METTL14, R298 is the most frequently mutated residue in samples from patients with cancer, and the mutant allele is observed along with the wild type (WT) (fig. S1, A and B) (*14*). Previous studies proposed that lower activity or aberrant specificity of the METTL14^{R298P} mutant leads to loss of canonical m^{6}A and the associated effects (*7*, *15*). However, the potential gain of function (GOF) of the cancer mutation has not been described. A novel function for the mutation would explain the observed enrichment of cancer mutations of METTL14^{R298}. Here, we show that R298P in METTL14 is a GOF mutation that promotes oncogenic cell growth compared to WT or the D312A loss-of-function (LOF) mutant. R298 mutants gain preference for RNA substrates containing GGAU over the canonical GGAC sequence in vitro and in the transcriptome. The overall m^{6}A levels are similar between the GOF and LOF mutants, highlighting the importance of the precise locations of m^{6}A marks for oncogenesis. We identified unique gene expression patterns in the cells expressing METTL14^{R298P}, especially for WNT signaling and additional cancer-related pathways. At the molecular level, the novel m^{6}A generated by the R298 mutant is detected by the YTH family of reader proteins similarly to the m^{6}A generated by the WT methyltransferase, but the mutant-generated m^{6}A is more resistant to demethylation by ALKBH5. Crystal structures of the GOF mutant METTL3-METTL14 methyltransferase domain complexes provide a model for how METTL14 helps recognize RNA substrate sequence.

RESULTS

METTL14^{R298P} causes malignant cell growth in culture and mice

The frequency of mutations at R298 of METTL14 in tumor samples led us to hypothesize that R298 mutations may have GOF effects that promote oncogenesis. To test the difference between WT and mutant METTL14, we generated four stable HepG2 liver cancer cell lines by integrating lentivirus cassettes expressing enhanced green fluorescent protein (EGFP), METTL14^{WT}, METTL14^{R298P}, or METTL14^{D312A} (fig. S1, C and D). D312A is spatially located close to R298P but is not derived from patients with cancer, and both mutations reduce methylation activity on canonical substrates containing the GGAC motif (*4*). We could not establish a null background or homozygous mutation of the METTL14 gene in HepG2 cells despite multiple attempts with genome-editing techniques due to loss of cell viability. Nevertheless, overexpressing mutant METTL14 alleles as EGFP fusion constructs allowed us to assess their role in a meaningful way because METTL14 and METTL3 need to heterodimerize to form an active methyltransferase—Heterologously expressed EGFP-METTL14 competes against the endogenous WT METTL14 for a limited amount of endogenous METTL3. Furthermore, heterozygous expression of mutant METTL14 more closely recapitulates the

[1]Department of Biochemistry, Department of Biophysics, Simmons Comprehensive Cancer Center, University of Texas Southwestern Medical Center, Dallas, TX 75390, USA. [2]Children's Research Institute, Departments of Pediatrics and Internal Medicine, Center for Regenerative Science and Medicine, University of Texas Southwestern Medical Center, Dallas, TX 75390, USA. [3]Eugene McDermott Center for Human Growth and Development, Department of Bioinformatics, University of Texas Southwestern Medical Center, Dallas, TX 75390, USA. [4]Department of Chemistry, University of California at Riverside, Riverside, CA 92521, USA. [5]Department of Pathology, University of Texas Southwestern Medical Center, Dallas, TX 75390, USA.
*Corresponding author. Email: yunsun.nam@utsouthwestern.edu

tumor samples since the R298 mutation is found along with the WT in RNA sequencing (RNA-seq) analyses of the tumor samples (cBioPortal). We verified that METTL14 fused to EGFP supports similar in vitro methylation activity as the WT gene (fig. S1E). None of the stable cell lines exhibited increased global m^{6}A levels, likely because of the limited amount of endogenous METTL3 (fig. S1F). For cells expressing METTL14^{R298P} or METTL14^{D312A}, overall m^{6}A levels of mRNAs were lower than WT, resembling an LOF phenotype without additional information (fig. S1G). Thus, we observed a decrease in overall mRNA m^{6}A in liver cancer cells with METTL14^{R298P}, similar to a previous study that used endometrial cancer cells (*7*).

To investigate how the R298 mutation affects cell growth, we compared cell proliferation, migration, and invasion of the four stable HepG2 cell lines expressing different METTL14 alleles. While the cell proliferation rate was unaffected by the mutations (fig. S1H), cells expressing METTL14^{R298P} showed increased capacity to migrate and invade (Fig. 1, A and B). In contrast, cells expressing METTL14^{D312A} behaved similarly to the ones expressing the WT protein. The R298P mutation is frequently found in endometrial cancer, and we also observed increased cell migration when the GOF mutant was expressed in HEC-1A cells (fig. S1, I and J). Therefore, we observed a more aggressive cell growth in cultured cells when METTL14^{R298P} was expressed, relative to the cells expressing the WT methyltransferase or the D312A LOF mutant.

We then asked how the changes in cell migration and invasion might affect tumorigenesis in animals. We used hydrodynamic transfection (HDT) to genomically integrate transposons containing METTL3 and METTL14 into mouse livers. To detect differences between WT and mutant METTL14 constructs, we used mice with a unique genetic background (liver-specific *Albumin-Cre*; *Tp53*$^{Fl/Fl}$; *Lin28a*$^{Fl/Fl}$; *Lin28b*$^{Fl/Fl}$) to tune tumorigenesis (Fig. 1C). Overexpression of METTL3 and METTL14^{R298P} resulted in larger and more frequent tumors than those injected with METTL3 and METTL14^{WT} (Fig. 1, D to F). Tumors in the METTL14^{R298P}-injected group affected a greater portion of the liver, where much of the normal tissue was replaced (Fig. 1F). The tumors in mice with METTL14^{R298P} also caused an ~fourfold increase in liver mass when compared to the animals injected with the WT or D312A variants of METTL14 (Fig. 1D). Histological examination revealed multiple tumors with sarcomatoid features, including atypical, spindly tumor cells with pleomorphic nuclei and increased mitoses (Fig. 1E). Compared to the tumors associated with METTL14^{WT} or METTL14^{D312A}, METTL14^{R298P} tumors were larger and replaced much of the hepatic parenchyma. In addition, the sarcomatoid tumors from the mice injected with METTL14^{R298P} showed areas of tumor necrosis, indicative of increased tumor aggressiveness. Therefore, the R298P mutation of METTL14 drives a more malignant growth phenotype than the WT protein in cultured cells and in mice.

To better understand the oncogenic phenotype, we used RNA-seq analysis to examine the gene expression changes unique to the R298P cell line. Gene ontology (GO) analysis using Ingenuity Pathway Analysis revealed that genes in certain pathways are consistently differentially expressed in all three pairwise comparisons with R298P (Fig. 1, G and H). Most notably, the WNT signaling pathway is inhibited in R298P cells compared to the other three cell lines, and multiple groups of genes involved in cell movement or invasion are up-regulated. We confirmed differential expression of certain genes in these top GO term groups using quantitative reverse transcription polymerase chain reaction (PCR) (Fig. 1, I and J). The proteins differentially expressed in cells expressing METTL14^{R298P} compared to the other cell lines can be mapped to similar top GO categories as in the RNA-seq analysis despite the lower coverage (fig. S2). Because METTL14^{R298P} expression causes unique gene expression and aggressive growth phenotypes when compared to the WT or another LOF mutant, we surmised that R298 mutations may furnish the methyltransferase with a novel function.

METTL14^{R298P} promotes m^{6}A modification at distinct sites in the transcriptome

To determine how the R298P mutation affects the methyltransferase activity, we investigated the changes in m^{6}A modification profiles in the transcriptome. We used the m^{6}A-seq workflow to detect the m^{6}A sites in polyadenylated RNAs (*10*, *11*). While there are other methods that can locate the methylation marks at a higher resolution than m^{6}A-seq (*16*–*18*), most of them rely on the presumed sequence near the modification site—Cyt immediately following the methylated Ade. However, such methods would arbitrarily prevent the detection of modified adenines in different sequence contexts. METTL3-METTL14 structures exhibit a prominent basic patch in METTL14 that may be used to bind RNAs (*4*, *5*, *19*). Because of the proximity of the R298P mutation to the putative RNA binding patch, we wanted to include the possibility that the mutation may cause a change in the RNA substrate sequence preference. Thus, to avoid bias regarding the sequence composition of the modification sites, we only relied on the affinity for m^{6}A antibodies to detect methylation events.

From each cell line expressing a unique METTL14 allele, we identified ~5000 to 7000 total m^{6}A-seq peaks that are reproduced in all three biological replicates (Fig. 2A). Each sample usually yields >10,000 peaks per replicate using our stringent peak-calling criteria. The inherently incomplete coverage of the m^{6}A-seq method results in fewer peaks reproduced in all replicates, but the peak overlap is in the expected range (*20*). Among the tested samples, the m^{6}A peaks in the cells expressing METTL14^{R298P} seem to overlap less with the peaks found in the other samples (fig. S3A). To dissect the difference among the METTL14 alleles, we identified peaks unique to each cell line by selecting the peaks that do not overlap with the peaks in the other three cell lines in a four-way comparison (Fig. 2A). The distribution of the unique and total peaks is similar genome-wide and within mRNAs (fig. S3, B and C). However, the m^{6}A peaks unique to R298P cells exhibit a different consensus sequence; R298P causes a preference for Ura after the methylated Ade, while the other samples retain the dominant Cyt signal at the same position (Fig. 2B). The changed preference for Ura is less prominent when all m^{6}A sites are analyzed, which may be due to the background from endogenous WT METTL14 (fig. S3D). Thus, we observed a distinct sequence enrichment only when we analyzed the m^{6}A peaks uniquely found in cells expressing METTL14^{R298P}.

To investigate the altered substrate specificity of METTL14^{R298P} further, we used a distinct method to identify the novel m^{6}A peaks that increase intensity upon expressing the GOF mutant. We compared the height of each m^{6}A peak to the signal in the EGFP control at the same genomic location (Fig. 2C). We then used the sequences with different relative peak heights (top or bottom 5%) for consensus motif analysis (Fig. 2D). For the R298P sample, the tallest peaks relative to the EGFP control (top 5%) showed a clear preference for Ura at the fourth position, but the shorter peaks compared to the EGFP control (bottom 5%) maintain a preference for Cyt at the fourth position (fig. S3E). No such difference in sequence preference was

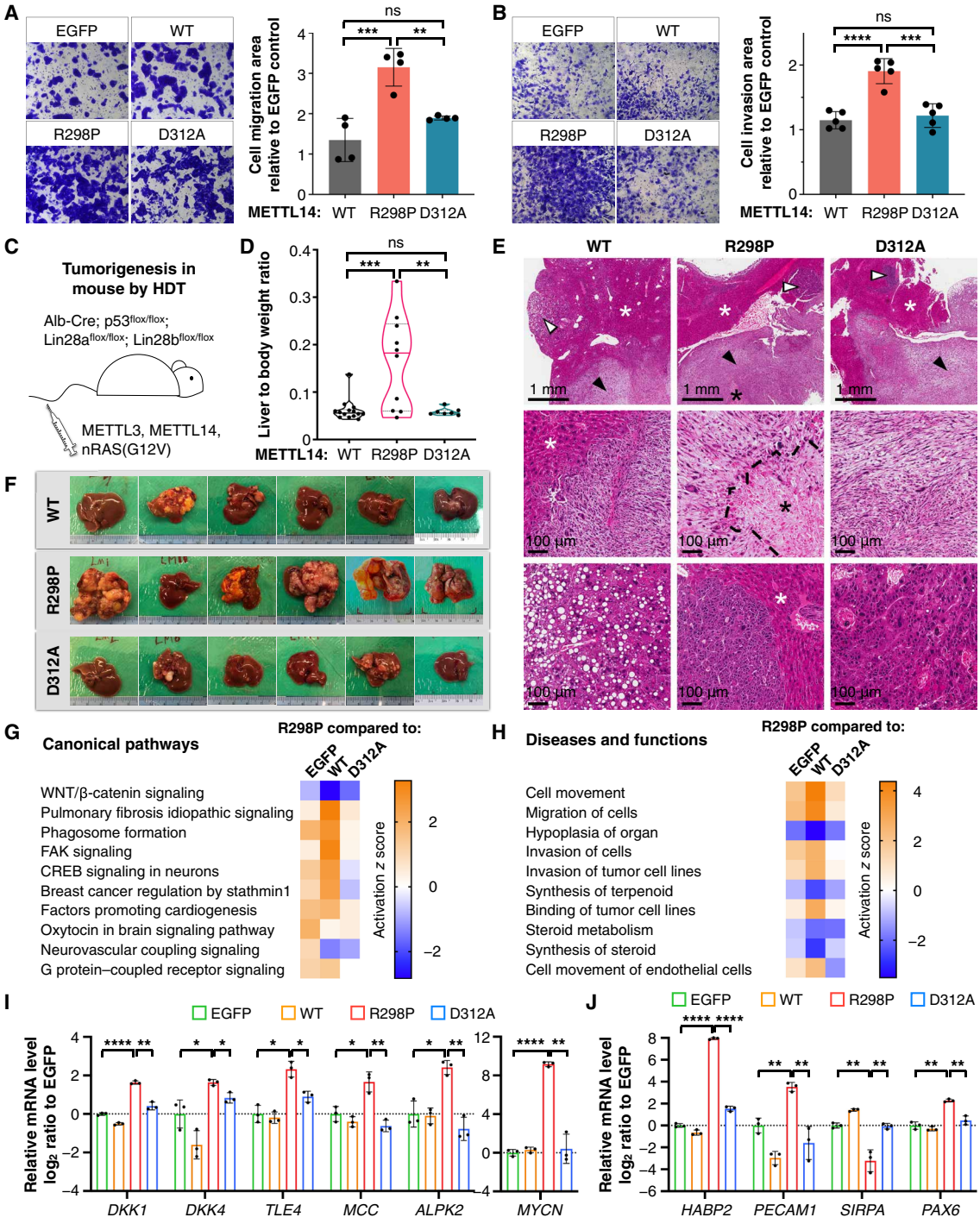

Fig. 1. METTL14^{R298P} causes more malignant cell growth in culture and mice. (**A** and **B**) Cell migration (A) and invasion (B) assays using HepG2 stable lines expressing EGFP or EGFP-METTL14 variants (WT, R298P, or D312A). Data are shown as means ± SD from four (A) or five (B) biological replicates normalized to EGFP. Ordinary one-way analysis of variance (ANOVA): ns, not significant; $^{**}P < 0.01$; $^{***}P < 0.001$; $^{****}P < 0.0001$. (**C**) Schematic of the mouse tumorigenesis assay via HDT. (**D**) Liver-to-body weight ratio of 84-day-old mice (42 days after injection) from 2 to 3 cohorts [14 WT, 10 R298P (excluding 2 deceased), or 7 D312A]. Data are shown as median with quartiles. Ordinary one-way ANOVA: ns, not significant; $^{**}P = 0.0025$; $^{***}P = 0.0005$. (**E**) Photomicrographs of mouse livers from tumorigenesis assay. Top, necrosis (black asterisk) seen only in R298P mice. Hepatic parenchyma (white asterisks) replaced by sarcomatoid features (black arrowheads) and epithelioid tumors (white arrowheads) are in all three. Middle, sarcomatoid tumors in higher magnification. Necrosis (black asterisk; with dashed border) is prominent in R298P. Bottom, epithelioid tumors in higher magnification. (**F**) Representative whole liver and tumor tissue images. (**G** and **H**) RNA-seq ($n = 3$) differential expression analysis by Ingenuity Pathway Analysis (IPA) Canonical pathways (G) and diseases and functions (H) modules. *Z* score for each GO term is shown (positive for activation or negative for inhibition in R298P cells). (**I** and **J**) Quantitative reverse transcription PCR of differentially expressed transcripts involved in WNT pathway (I) and cell movement (J). Data are shown as means ± SD of normalized (to EGFP) **Δ**Cp values from three biological replicates. Two-tailed *t* test: $^{*}P < 0.05$; $^{**}P < 0.01$; $^{****}P < 0.0001$.

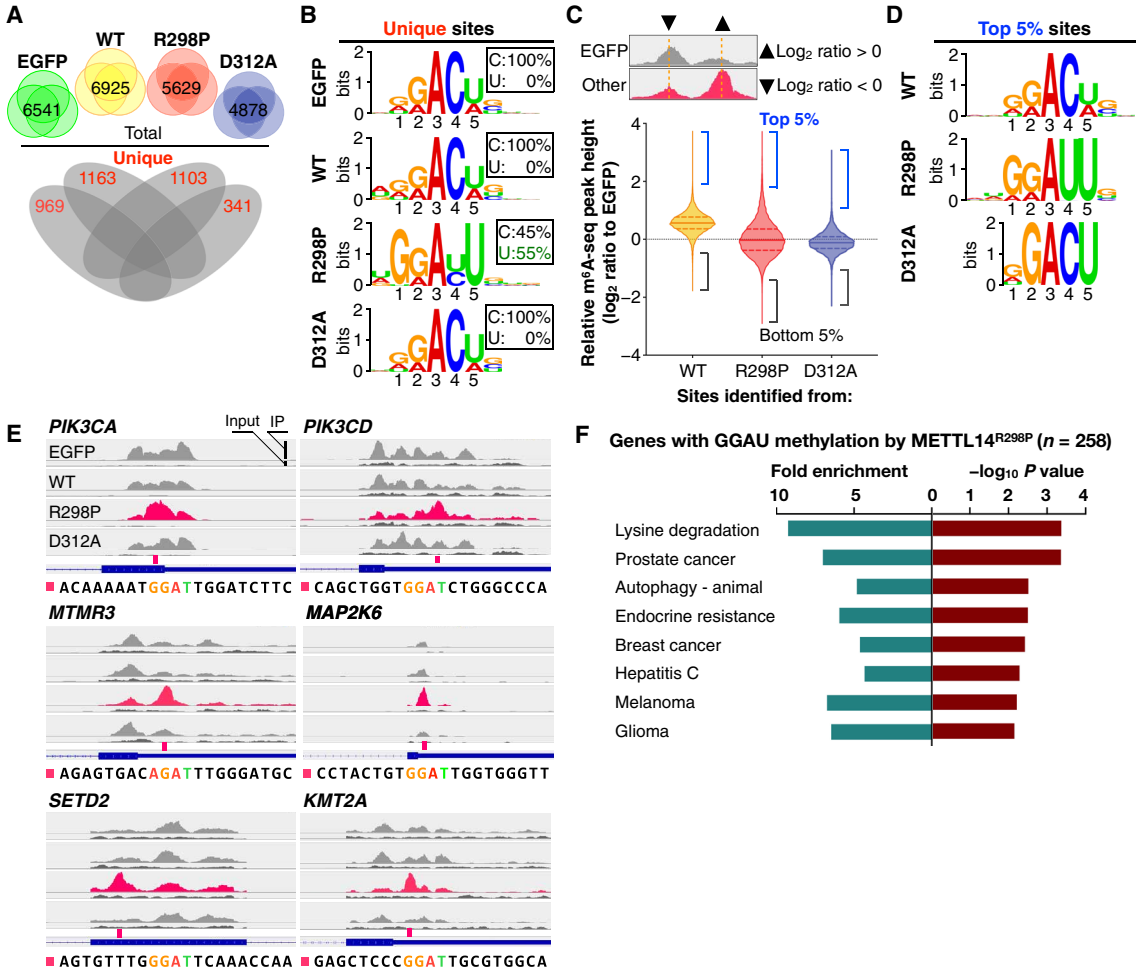

Fig. 2. METTL14^{R298P} promotes m^{6}A modification of distinct RNA sites in the transcriptome. (**A**) HepG2 stable lines expressing EGFP or METTL14 (WT, R298P, or D312A) were used for m^{6}A-seq. The number of peaks reproduced in three replicates of each cell line is shown as an intersection on top (total, black font), and the unique peaks after a four-way comparison are shown below (unique, red font). (**B**) Motif analysis of the m^{6}A sites unique to each cell line [red numbers in (A)]. The probability percentages of Cyt and Ura at the fourth position are shown in boxes. MEME *P* values from top to bottom: 2.2×10^{-119}, 8.7×10^{-75}, 5.6×10^{-103}, and 8.8×10^{-21}. (**C**) m^{6}A-seq peak height relative to the EGFP. Schematic of the summit signal comparison workflow is shown on top. Data are shown as median and quartiles with $n = 33549$ (WT), 28892 (R298P), or 26703 (D312A). The brackets mark the top or bottom 5 percentiles. (**D**) Motif analysis of the top 5% methylation sites [blue brackets in (C)]. MEME *P* values from top to bottom: 7.4×10^{-81}, 7.7×10^{-349}, and 1.1×10^{-21}. (**E**) Browser tracks of example transcripts with a peak unique to METTL14^{R298P} (pink). The peak location (pink tick mark), sequence, and methylation site (colored) are indicated. (**F**) GO analysis (DAVID) of the genes ($n = 258$) that contain at least one m^{6}A peak unique to R298P cells (Fig. 2A) and one tall m^{6}A peak (top 5%, relative to EGFP) (Fig. 2C).

observed for the other cell lines. The peaks included in this analysis have different relative heights compared to those of the EGFP control, but the actual normalized peak height has a similar distribution in both (fig. S3F). Manual inspection of the m^{6}A-seq gene-browser tracks of the "top 5%" peaks provided examples of the peaks that are taller in R298P cells, and we can readily identify the signature sequence preference of the GOF mutant, GGAU (Fig. 2E and fig. S3G). We performed GO analysis on the most stringent set of R298P-dependent novel m^{6}A peaks—the peaks that are taller in R298P (top 5%) and lack overlap with m^{6}A peaks from any of the other samples (R298P-unique). The most robust sites targeted by METTL14^{R298P} happen to be involved in histone modification and cancer pathways (Fig. 2F and fig. S3G). How the novel methylation by the GOF mutant methyltransferase leads to altered gene expression important for cancer, including changes in WNT signaling and cell motility, needs further investigation and may change with different cellular contexts. At the molecular level, by comparing the differential methylation of the transcriptome in four different cell lines, we conclude that METTL3-METTL14^{R298P} generates novel m^{6}A peaks in the transcriptome, preferentially at GGAU rather than GGAC sites.

METTL14^{R298P} prefers noncanonical GGAU sequences

The METTL3-METTL14 complex interacts with many other factors in the cell, including WTAP, VIRMA, RBM15, ZC3H13, and HAKAI (*3*, *21*–*26*). We postulated that the R298P mutation rewires the intrinsic RNA substrate specificity of METTL3-METTL14 independent of other factors. To determine the substrate specificity in an unbiased fashion, we developed the in vitro methylation sequencing (IVM-seq) workflow by adopting the strategies from the systematic evolution of ligands by exponential enrichment (SELEX) approach

(Fig. 3A) (*27*). IVM-seq allows us to perform a deep search of the sequence space because the complexity of the initial randomized RNA pool (approximately 1×10^{12}) is higher than that of a typical transcriptome. In contrast to SELEX that relies on protein-RNA binding affinity to enrich for the cognate RNA sequence, we first allowed the recombinant methyltransferase to modify the RNA pool and then selected the methylated molecules using an m^{6}A-specific antibody. The high-throughput sequencing results were then analyzed to derive the consensus motif (Fig. 3B). The preferred sequence of the WT methyltransferase, GGAC, resembled the canonical DRACH motif (*10*, *11*). In contrast, a distinct consensus sequence—GGAU—was derived for METTL3-METTL14^{R298P}. IVM-seq analysis of other R298 mutants (R298C and R298H, both found in patients) yielded similar motifs where Ura is preferred over Cyt at the fourth position. Thus, a single amino acid substitution was sufficient to dramatically alter the preferred nucleobase at the fourth position, from Cyt to Ura, changing the consensus motif from GGAC to GGAU. METTL3-METTL14^{D312A} maintained a clear preference for Cyt over Ura at

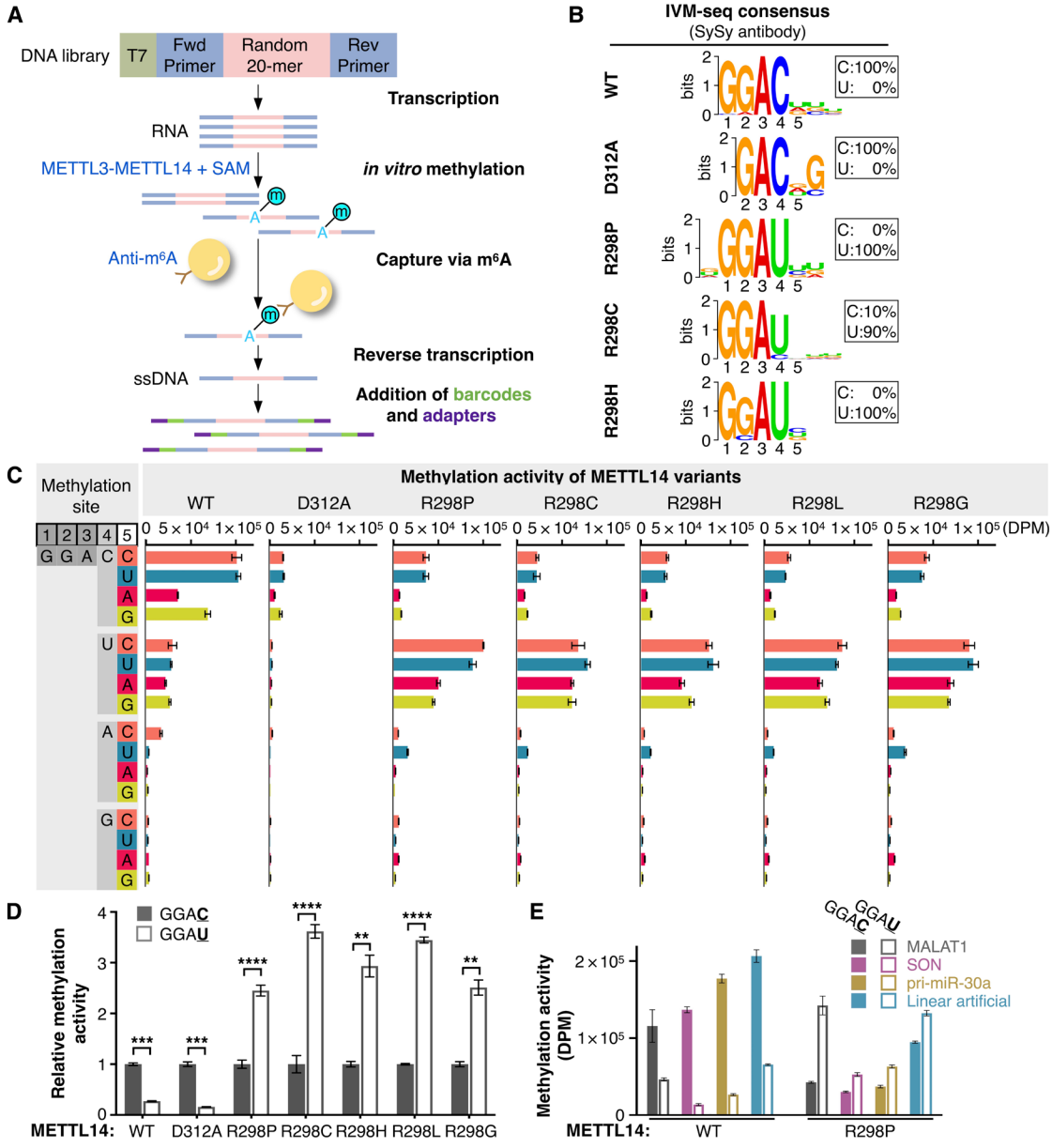

Fig. 3. METTL14^{R298P} prefers noncanonical GGAU sequences. (**A**) Workflow for IVM-seq. Oligonucleotides with a 20-nt randomized segment are used to generate the RNA pool for in vitro methylation. Methylated RNAs selected by an anti-m^{6}A antibody are subjected to high-throughput sequencing. (**B**) Motif analysis of the IVM-seq output for RNAs methylated by the METTL3-METTL14 complex variants. MEME *P* values from top to bottom: 5.2×10^{-412}, 4.6×10^{-7}, 4.0×10^{-355}, 6.5×10^{-1771}, and 6.9×10^{-1094}. (**C**) In vitro methylation activity of recombinant METTL3-METTL14 variants, on a series of RNA fragments derived from *MALAT1* (with single nucleotide changes at fourth or fifth positions). Methylation activity is represented by the amount of tritium transferred from SAM (S-[methyl-^{3}H]) to RNA, measured as DPM by scintillation counting. (**D**) In vitro methylation activity of the GGAU substrate normalized to GGAC for each METTL14 variant. Two-tailed *t* test: $^{**}P < 0.01$; $^{***}P < 0.001$; $^{****}P < 0.0001$. (**E**) In vitro methylation of RNA substrates in different sequence and structural contexts. Data represented as means ± SD from three replicate reactions in (C) to (E).

the fourth position, although the overall low methylation activity made it difficult to determine the sequence preference at the first position. Therefore, METTL14^{D312A} is clearly an LOF mutation that causes lower methylation for both normal and other targets, whereas the GOF R298 mutations gain increased methylation activity for GGAU targets. To test for potential bias introduced by a particular antibody, we used multiple anti-m^{6}A antibodies produced by different companies, but the antibody source did not change the sequence preference derived from IVM-seq (fig. S4A). Using the same randomized RNA library, we also performed SELEX to identify the RNA sequences that bind the methyltransferase more tightly. Unlike IVM-seq, we could not identify a clear consensus sequence for the best binders of METTL3-METTL14 (fig. S4B). The altered sequence preference may be more relevant for catalysis than for binding. Therefore, we established robust methods to determine the sequence preference of an RNA m^{6}A methyltransferase in an unbiased manner, and we determined that R298 substitutions transform the methylation substrate specificity of METTL3-METTL14 independent of other factors.

To investigate the altered RNA specificity of the isolated METTL3-METTL14 methyltransferase using an orthogonal approach, we used a quantitative enzymatic assay where an established canonical m^{6}A site sequence in the *MALAT1* noncoding RNA was changed at every position (Fig. 3C) (*28*). For the recombinant methyltransferase, we tested patient-derived mutants and additional substitutions that can be obtained through a single nucleotide change. The WT enzyme consistently shows a strong preference for Cyt at the fourth position, although some methylation activity is observed for substrates with Ura in the fourth position. In contrast, the substrate preference was reversed for METTL3-METTL14^{R298X} mutants because GGAU substrates were methylated more efficiently than GGAC substrates. The mutant enzyme activity on GGAU substrates was comparable to the WT enzyme on the normal sites containing GGAC as indicated by the raw disintegration per minute (DPM) counts. The fifth position is not as discriminatory, but pyrimidines are generally preferred by both WT and mutant enzymes. For methyltransferase complexes containing METTL14^{WT} or METTL14^{D312A}, the preference for GGAC over GGAU is 3.7- or 6.3-fold, respectively (Fig. 3D). In contrast, all R298 mutations of METTL14 reverse the sequence preference, where having Ura at the fourth position increases methylation by 2.4- to 3.6- fold compared with Cyt. While the sequence seems important, the structural context may also affect RNA methylation efficiency (*29*). Thus, we tested three other RNA scaffolds derived from a known mRNA target (SON), a primary microRNA (pri-miR-30a), and an artificial sequence predicted to lack secondary structure (Fig. 3E and fig. S4, C and D). Different scaffolds affect methylation activities, but the WT enzyme consistently modifies GGAC more efficiently than GGAU, while the R298P mutant has the opposite sequence preference. Different substrate binding affinities could explain the altered methylation substrate preference, although SELEX was unable to detect a clear consensus (fig. S4B). In electrophoretic mobility shift assays (EMSA), the WT and mutant enzymes exhibit similar affinities for RNA substrates containing GGAC or GGAU motifs (fig. S4E). Thus, the observed changes in methylation are not due to a different association efficiency with the RNA substrate. Furthermore, the affinity for the methylated RNA is also similar (fig. S4F), suggesting that product release is not the step affected by R298P. Together, quantitative enzymatic assays and binding assays show that METTL14^{R298P} changes the substrate sequence preference for methylation, without affecting binding affinities.

METTL14^{R298P}-generated m^{6}A is more resistant to demethylation by ALKBH5

Given the remarkable effect of a change in sequence preference for the methyltransferase, we asked how the sequence contexts affect the molecular fate of the m^{6}A modification. Most m^{6}A marks rely on being recognized by a reader protein for effector function (*1*, *2*). We tested whether the novel methylated sequence, GGm^{6}AU, would interfere with binding the canonical reader proteins containing YTH domains. We used purified recombinant YTHDC1, YTHDC2, YTHDF1, YTHDF2, and YTHDF3 (fig. S5A) to test how the sequence context affects the affinity of the YTH proteins to m^{6}A-modified RNA. The YTH domains derived from all five readers bind more tightly to the methylated RNAs compared to the unmethylated RNA in gel-shift assays, and the affinity for the m^{6}A-modified RNA can vary (Fig. 4A and fig. S5B). Changing the sequence context from GGAC to GGAU did not alter the ability of each reader protein to detect the m^{6}A modification. Thus, the m^{6}A modifications created by METTL14^{R298P} at noncanonical sites containing GGAU can recruit m^{6}A readers similarly to the canonical m^{6}A sites containing GGAC (*30*).

Fat mass and obesity-associated protein (FTO) and AlkB family member 5 (ALKBH5) can demethylate m^{6}A marks to revert them back to adenosines (*31*, *32*). We asked how the sequence context affects RNA interactions with the m^{6}A erasers, FTO and ALKBH5. Unlike the YTH proteins, ALKBH5 and FTO showed similar binding to both unmethylated and methylated RNA substrates, and the sequence context did not substantially change the affinities (Fig. 4B and fig. S5C). We also measured how the demethylation activities change with RNA sequence. FTO demethylates both RNA substrates similarly (Fig. 4C), but ALKBH5 shows higher efficiency in demethylating GGAC previously methylated by WT METTL3-METTL14 than GGAU previously methylated by METTL3-METTL14^{R298P} (Fig. 4D). Our findings add to the structure-based studies that reported the sequence preference of ALKBH5 as RAC (*33*). ALKBH5 is expressed at similar levels across the different HepG2 cell lines we have established (fig. S5, D and E). Therefore, we conclude that a key difference in the molecular fate of the m^{6}A marks created by METTL3-METTL14^{R298P} is the innate resistance to the demethylase ALKBH5.

Structural basis for altered RNA specificity of METTL14^{R298P}

To build a molecular model to understand the novel RNA target specificity of METTL14^{R298X}, we determined crystal structures of the methyltransferase domain complexes of METTL3-METTL14, for all three patient-derived mutations of R298 in METTL14 (table S1). In the WT elongated heterodimeric complex, R298 of METTL14 is located >20 Å away from the bound *S*-adenosyl methionine (SAM) in the active site of METTL3 (Fig. 5A). In all three mutant structures, the overall backbone conformation of both proteins is similar to WT, but certain important side-chain rearrangements occur. Superimposing the WT structure on that of METTL3-METTL14^{R298P} shows that R471 and H474 of METTL3 move inward to fill the space that is normally occupied by the side chain of METTL14^{WT} R298 (Fig. 5B). For structures containing R298H or R298C mutations in METTL14, we observe electron densities that suggest that both conformations are accessed by the same two residues (Fig. 5C and fig. S6, A to D). Therefore, we conclude that the loss of the arginine side chain at 298 allows the protein to default to an alternative conformation that preferentially methylates GGAU sequences.

Because of the alternative conformations in the mutant structures, we postulated that R471 and H474 in METTL3 are likely to

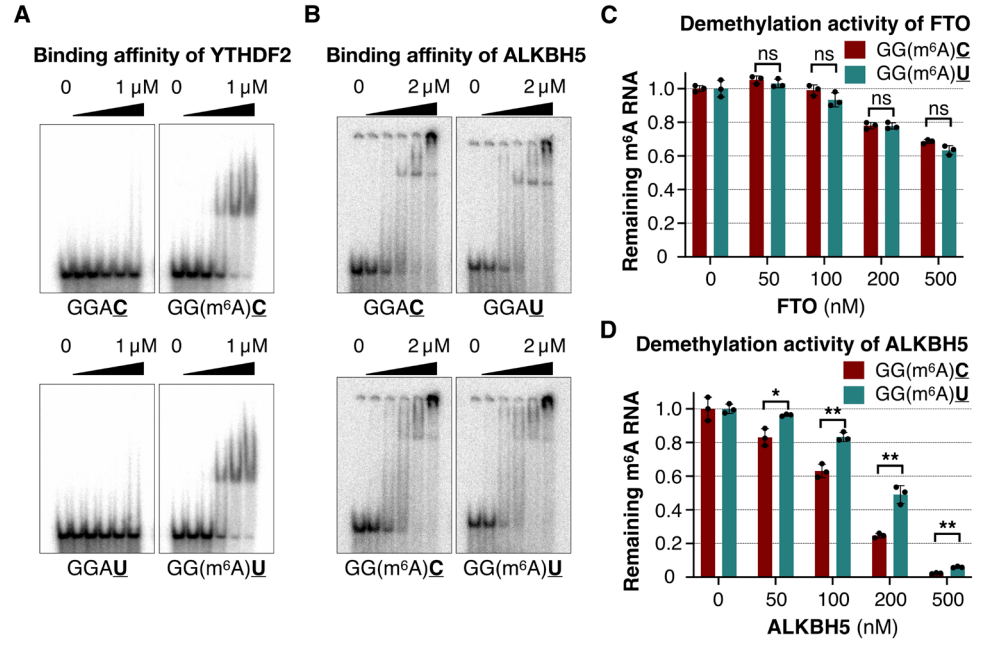

Fig. 4. METTL14^{R298P}-generated m^{6}A is more resistant to demethylation by ALKBH5. (**A** and **B**) Gel-shift assay of YTHDF2 and ALKBH5 with RNA containing GGAC or GGAU with or without m^{6}A modification. Protein concentrations in (A) are from left to right, 0, 0.065, 0.130, 0.260, 0.521, and 1.04 μM. Protein concentrations in (B) are from left to right, 0, 0.130, 0.260, 0.521, 1.04, and 2.08 μM. (**C** and **D**) Quantitation of in vitro demethylation activity of FTO and ALKBH5 on methylated RNAs (0.5 μM). The activity is represented as the percentage of tritium (methyl-^{3}H) remaining after demethylation. Data represented as means ± SD from three replicate reactions. Two-tailed *t* test: *$P < 0.05$; **$P < 0.01$; ns, not significant.

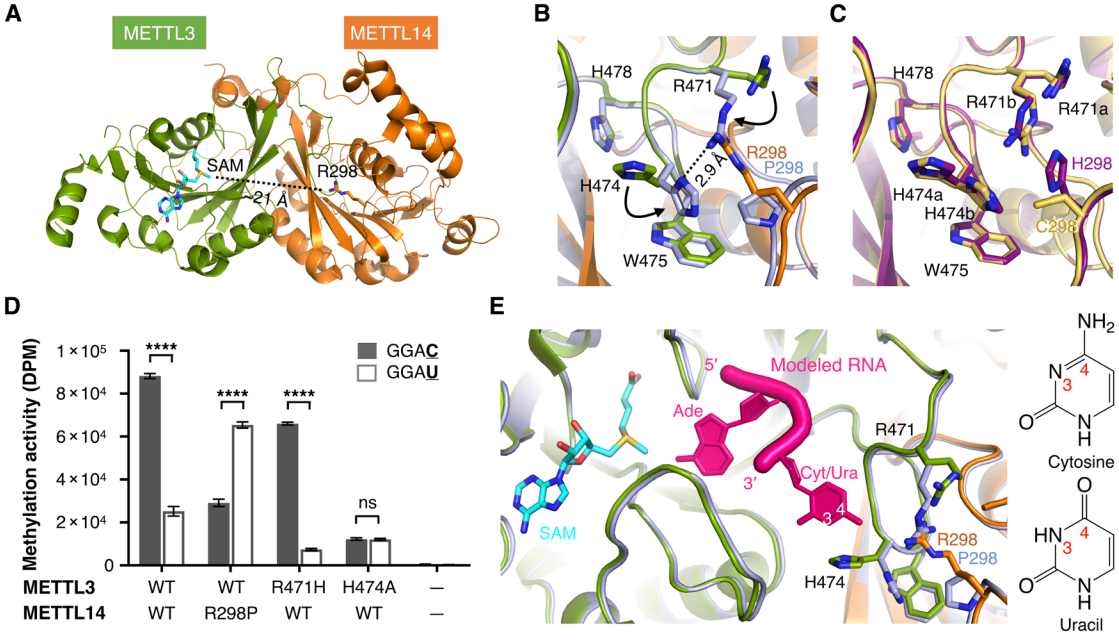

Fig. 5. Structural basis for the novel specificity of METTL14 mutants. (**A**) Overall structure of WT METTL3-METTL14 methyltransferase domains provided for context, and SAM (cyan) and R298 side chain are shown with stick representation. (**B** and **C**) Close-up views of the METTL3-METTL14 complex crystal structures near the interface. WT (green and orange) superimposed on R298P (light blue) (B) and R298C (yellow) superimposed on R298H (purple) (C) in the same orientation. METTL3 residues are labeled in black. For (C), two alternative conformations could be modeled for two residues. (**D**) In vitro methylation assay of indicated mutant proteins using RNA containing GGAC or GGAU. Data are shown as means ± SD from triplicates. Two-tailed *t* test: ****$P < 0.0001$; ns, not significant. (**E**) Model of RNA (pink) containing Ade (to be methylated to m^{6}A) and the next nucleotide bound to superimposed structures of WT METTL3 (green or light blue) in complex with METTL14^{WT} (orange) or METTL14^{R298P} (gray). Positions 3 and 4 (white) of the pyrimidine ring in Cyt or Ura (chemical structures shown on right) may be distinguished via the observed side-chain rearrangements.

contribute to the changed nucleobase preference at the fourth position. We introduced point mutations and measured the in vitro methylation activity (Fig. 5D). Both mutations affect the relative preference between GGAC and GGAU substrates, although in opposite directions, indicating that they contribute to recognizing the nucleotide immediately following the methylated Ade. R471H mutation of METTL3 has been observed in patients with cancer, raising the possibility that the RNA specificity of METTL3-METTL14 may be altered in multiple ways to contribute to disease.

Combining our structural and biochemical data, we modeled how RNA substrates bind near the active site of METTL3-METTL14 (Fig. 5E). The methylated adenine can be placed near the SAM binding site by superimposing the RNA-bound structure of another m^{6}A writer enzyme, METTL16 (*29*). Abiding by the RNA geometry constraints, the adjacent nucleotide can be modeled to contact H474 and R471 of METTL13 or R298 of METTL14, within hydrogen-bonding distance, depending on the side-chain conformations. Cyt and Ura differ at positions 3 and 4 of the pyrimidine ring, and R471 and H474 of METTL3 and R298 of METTL14 together accomplish the normal RNA selectivity profile of METTL3-METTL14. Therefore, while investigating the molecular rationale for the oncogenic phenotype of a GOF mutant, we were also able to gain insight into how RNA substrates normally engage with WT METTL3-METTL14 near the active site.

DISCUSSION

Our work uncovers how a point mutation in METTL3-METTL14 can transform the RNA methylation substrate specificity and promote oncogenesis. Mutations of METTL14^{R298} change the sequence preference of the m^{6}A writer complex, METTL3-METTL14. While the WT prefers GGAC over GGAU, the mutant exhibits the reversed substrate preference (Fig. 6). The particularly aggressive growth of cells expressing METTL14^{R298P} is associated with gene expression changes in the WNT/β-catenin signaling pathway and others known to control cell migration and invasion. The m^{6}A modifications of GGAU sites generated by R298 mutants can be recognized by the YTH family of reader proteins similarly to the canonical GGAC sites. However, the noncanonical m^{6}A in GGAU is not as efficiently demethylated by the eraser ALKBH5, indicating that the sequence context can affect the function and metabolism of m^{6}A (*32*, *34*). Our work leads to an atomic model to elucidate how METTL3-METTL14 recognizes RNA substrates by combining the structural and biochemical data. Together, we have unveiled the molecular mechanism underlying a cancer mutation as well as the normal recognition of RNA substrates for METTL3-METTL14.

Overexpression of WT METTL3-METTL14 and hypermethylation has been implicated in cancers. We show that a changed methylation pattern can promote oncogenesis without increasing global m^{6}A levels in mRNAs. R298P and D312A mutations of METTL14 both decrease the level of m^{6}A modification in mRNAs to similar extents, but only R298P promotes oncogenic phenotype compared to D312A or WT. Therefore, the novel methylation activity of the R298P mutant with GGAU-containing targets is likely responsible for the increased oncogenesis. R298 is most frequently mutated within the METTL14 gene among tumor samples but not as much as some well-known tumor suppressor genes. Given that the WT methyltransferase has appreciable activity on the less preferred GGAU sequence (Fig. 3C) (*35*, *36*), overexpressed METTL3-METTL14 likely also increases noncanonical methylation above a tolerable threshold. Thus, overexpression of WT METTL3-METTL14 may share a similar pathogenic mechanism as the GOF mutant, METTL3-METTL14^{R298P} in some contexts (red, Fig. 6). Many previous studies relied on the canonical m^{6}A signature (GGAC or DRACH) to locate and quantify m^{6}A modification and correlate it to oncogenesis. Our studies suggest a distinct mechanism where increased GGAU methylation is linked to more oncogenesis. Therefore, more attention to the m^{6}A site sequence contexts and location changes as well as m^{6}A metabolism is likely crucial to understanding its mechanistic role in cancer.

The gain of sequence preference for GGAU over GGAC was missed in previous studies of METTL14^{R298P}, partly because expression of METTL14^{R298P} also leads to loss of canonical methylation at GGAC sites (*7*, *15*). Furthermore, the overall methylation efficiency of METTL14^{R298P} is lower than the WT allele, leading to globally lower m^{6}A levels in mRNAs (fig. S1G); without a focused analysis of unique or strong peaks, GGAC overshadows GGAU in

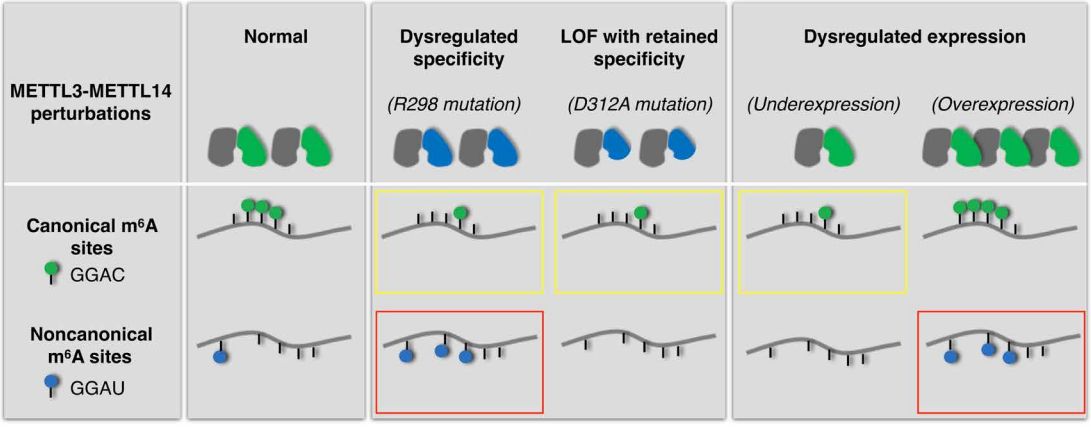

Fig. 6. Dysregulated METTL3-METTL14 can cause distinct m^{6}A modification states. Our study shows a distinct mechanism to dysregulate METTL3-METTL14 by rewiring its RNA substrate specificity. In normal conditions, WT METTL3-METTL14 prefers GGAC over GGAU. R298 mutations reverse the sequence preference. Lower than normal methylation at GGAC sites (yellow rectangles) is common to R298 mutants, LOF mutants, and methyltransferase under-expression. Higher than normal methylation at GGAU sites (red rectangles) is common to R298 mutants and methyltransferase overexpression, which have both been observed in multiple cancers.

transcriptome-wide m^{6}A consensus analysis. Thus, even when the rare cells homozygous for METTL14^{R298P} showed GGAU methylation, the activity was deemed as aberrant rather than a specific GOF (*15*). The oncogenic effect of METTL14^{R298P} can be due to increased GGAU methylation and decreased GGAC methylation (yellow, Fig. 6). How lower GGAC methylation might contribute to cancer was already reported previously (*7*). In our study, we highlight the dominant oncogenicity of GGAU m^{6}A sites by comparing METTL14^{R298P} to METTL14^{D312A}, an LOF mutant that generates similar m^{6}A levels in mRNAs without altering the substrate specificity.

GOF mutations that change how proteins interact with metabolites, proteins, or DNA have been shown to affect cancer (*37*–*39*). Our work shows a pioneering example of a point mutation that can rewire an RNA modification enzyme to recognize a distinct nucleotide sequence as the preferred substrate, revealing a powerful GOF mechanism that has not been previously recognized and that may be prevalent in the evolution of cancer cells. The diverged active site of the oncogenic mutant also likely opens avenues for targeted therapeutics with lower toxicity.

MATERIALS AND METHODS

Plasmid construction

For coexpression of human METTL3 and METTL14 recombinant protein in *Escherichia coli*, cDNA corresponding to full-length METTL3 (amino acids 1 to 580) and METTL14 (amino acids 1 to 456 and EGFP coding sequence fused to the N terminus in fig. S1E) were cloned into pETDuet vector in previous work (*4*). Point mutations were introduced by site-directed mutagenesis. For lentiviral constructs expressing METTL14^{WT}, METTL14^{R298P}, and METTL14^{D312A}, corresponding sequences were subcloned into the pLJM1-EGFP vector (Addgene, plasmid #19319) (*40*). To express human YTH, FTO, and ALKBH5 recombinant proteins in *E. coli*, the cDNA corresponding to YTHDC1 (amino acids 345 to 509), YTHDC2 (amino acids 1281 to 1430), YTHDF1 (amino acids 359 to 559), YTHDF2 (amino acids 383 to 579 and 1 to 579), YTHDF3 (amino acids 385 to 585), FTO (amino acids 1 to 505), and ALKBH5 (amino acids 66 to 394) were subcloned into the pET21a vector (Novagen). For lentiviral construct expressing short hairpin to knockdown endogenous METTL14^{WT}, the sequences listed in table S2 were subcloned into the EZ-Tet-pLKO-Puro vector (Addgene plasmid, #85966) (*41*) between NheI and EcoRI sites. For transient overexpression of METTL3 and METTL14, full-length METTL3 and METTL14^{WT}, METTL14^{R298P} and METTL14^{D312A} were cloned into pcDNA3.1 vector (Invitrogen). For the constructs used for mouse HDT, cDNA corresponding to full-length METTL3 and METTL14 with specific mutations were each subcloned into the pT3-EF1α vector.

Cell culture

Human liver cancer cell line HepG2 was obtained from American Type Culture Collection (ATCC, HB-8065). HepG2 cells were cultured in minimum essential medium (MEM) with Earle's Balanced Salt Solution (EBSS), 2 mM L-glutamine (Cytiva, SH30024) supplemented with 1% nonessential amino acids (Gibco, 11140-050), and 10% fetal bovine serum (FBS, Corning, 35-011-CV). The 293 Lenti-X cell line was a gift from D. Nijhawan (University of Texas Southwestern Medical Center). The 293 Lenti-X cells were cultured in Dulbecco's modified Eagle's medium (Sigma-Aldrich, D6429) supplemented with 10% FBS. Human endometrium cancer cell line HEC-1-A was obtained from ATCC (HTB-112). HEC-1-A cells were cultured in McCoy's 5A medium (Sigma-Aldrich M8403) supplemented with 1.5 mM L-glutamine (Sigma-Aldrich, G7513) and 10% FBS. All cell lines were cultured under standard mammalian cell culture conditions (37°C, 5% CO_2). All cell lines were tested to be Mycoplasma free by Lonza Walkersville Mycoplasma Testing Kit (Lonza, LT07118).

Virus production and generation of stable cell lines

To generate lentiviruses for overexpression of EGFP control, METTL14^{WT}, METTL14^{R298P}, and METTL14^{D312A}, each pLJM1 plasmid was cotransfected with psPAX2 (Addgene, plasmid #12260) and pMD2.G (Addgene, plasmid #12259) using Lipofectamine 3000 (Invitrogen L3000015) into the 293 Lenti-X cells. Viral particles–containing media were collected at 72 hours after transfection and filtered by 0.45-μm polyvinylidene difluoride (PVDF) syringe filter (Millipore, SLHVR33RS). For the generation of stable overexpression of EGFP control, METTL14^{WT}, METTL14^{R298P}, and METTL14^{D312A} HepG2 cell lines, 2.5 million cells were seeded on each 100-mm plate 24 hours before the viral transduction. The viral transduction was accomplished by incubating cells with a mixture of 10% (v/v) virus-containing media and complete growth media in the presence of Polybrene (10 μg/ml, Sigma-Aldrich, TR-1003-G) for 48 hours. Puromycin (1 μg/ml) was added to the growth media for selection. The selection lasted 8 days when fresh puromycin-containing media were provided every 48 hours. The HEC-1-A stable knock-down cell line was produced similarly. The short hairpin sequence containing EZ-Tet-pLKO-puro plasmid was cotransfected in the viral particle production. The knockdown of endogenous METTL14 was induced by doxycycline (50 ng/ml, Sigma-Aldrich, D5207) in media.

Quantification of global m^{6}A level by MS

Total RNA was extracted from 10 million cells using TRIzol (Invitrogen, 15596026) according to the manufacturer's instructions. RNA was digested with deoxyribonuclease I (DNase I, 10 U) at 37°C for 30 min and extracted by acid phenol–chloroform and precipitated by isopropyl alcohol before dissolving in nuclease-free water. Poly(A) RNA was selected from the total RNA with NEBNext Poly(A) mRNA magnetic isolation module (NEB, E7490L) using 100 μl of beads slurry per 100 μg of total RNA. Poly(A) RNA samples (200 ng) were denatured at 70°C for 5 min in a 20-μl digestion buffer (50 mM sodium acetate pH 5.5) before the incubation with 2 U of nuclease P1 (Sigma-Aldrich, N8630) at 42°C for 2 hours. The digested samples were mixed with 3 μl of ammonium bicarbonate (1 M), 1 μl of $MgCl_2$ (25 mM), and 5 U of Antarctic phosphatase (NEB, M0289S) and then incubated at 37°C for 2 hours. The samples together with serial dilutions of adenosine (0.05 to 5 μM, Sigma-Aldrich, A9251) and m^{6}A (1 to 100 mM, MCE, HY-N0086) were analyzed on RapidFire 300 high-throughput Solid Phase Extraction (SPE) system (Agilent Technologies) interfaced with a Sciex 6500 (Sciex). For RapidFire sample preparation, the load/wash solvent (solvent A) was water containing 0.1% trifluoroacetic acid. The elution solvent (solvent B) was acetonitrile/water (8:2, v/v) containing 0.1% trifluoroacetic acid. Samples were aspirated from 384-well plates and loaded onto an SPE cartridge (cartridge type C, C18) to remove buffer salts using solvent A at a flow rate of 1.5 ml/min for 3000 ms. The retained and purified analytes were eluted to the mass spectrometer by washing the cartridge with solvent B at 1.25 ml/min for 5000 ms. The cartridge was reequilibrated with solvent A for 600 ms at 1.5 ml/min. For spectrometer detection, adenosine and m^{6}A were measured using a selective

reaction monitoring protocol. The parent ions in Q1 and their corresponding daughter ions in Q3 were as follows: (i) Q1 mass = 268.2 amu > Q3 mass = 135.9 amu for adenosine, (ii) Q1 mass = 281.7 amu > Q3 mass = 149 amu for m^6A. The resolution for Q1 and Q3 were set to "unit." A dwell time of 150 ms was used for each transition. For adenosine detection, the declustering potential was set to 25 V, the entrance potential to 10 V, collision energy to 27 V, and collision cell exit potential to 16 V. For m^6A detection, the declustering potential was set to 36 V, the entrance potential to 10 V, collision energy to 19 V, and collision cell exit potential to 4 V. For both nucleosides, the ion spray voltage was set to 5500 V and the source temperature was 700°C. The gas settings were as follows: curtain gas (30-psi ion), source gas 1 (70 psi), and ion source gas 2 (70 psi). The area under the daughter ion peaks (area under the curve) was quantified using RapidFire integrator software. The absolute concentrations of adenosine and m^6A from each sample were determined by the standard curves generated from each serial dilution of the m^6A and A, and then the m^6A/A ratios were calculated. Mass spectrometry (MS) was performed, and data were collected at the Department of Biochemistry at University of Texas Southwestern Medical Center.

Cell invasion, migration, and proliferation assays

For HepG2 stable cell line invasion assay, the inserts (Corning, 354480) precoated with Matrigel were rehydrated with serum-free MEM with 1% nonessential amino acids for 2 hours in the cell culture incubator. A total of 150,000 cells per insert in serum-free MEM (0.5 ml) were seeded inside the insert, and another 0.5 ml of complete growth media was placed on the bottom of the well. Following 72-hour of invasion, the cells were fixed and stained in the crystal violet solution (5 mg/ml crystal violet, 20% methanol in water solution, filtered) for 30 min. The inserts were extensively washed in water, and the top side of inserts was rubbed by cotton swabs before air-drying. Four (under 5× objective) or eight images (under 10× objective) on different locations of the same insert were taken under the brightfield using an inverted microscope. Images were analyzed by ImageJ (*42*), and the percentage of areas with signal above the automatically determined threshold was quantified for each image. The average was calculated for each sample, and the normalization to the corresponding EGFP control was performed for each batch of experiments. Each batch of experiments at one time was considered a biological replicate. For the cell migration assay, similar procedures were followed except for using a non-coated insert (Corning, 353097). The migration assay for HEC-1-A cells was performed similarly, except that 75,000 cells were seeded per insert. The cell invasion and migration images of EGFP samples were only quantified to normalize the data; thus, they were not plotted or tested for statistical significance. For the proliferation assay, 5000 cells per well were seeded on 96-well plates and three replica plates were prepared on day 0. The number of viable cells was determined using CellTiter 96 AQueous One Solution Cell Proliferation Assay kit (Promega G3580), and absorbance at 490 nm was measured by a plate reader (CLARIOstar) on days 1, 3, and 5. The absorbance values from days 3 to 5 were normalized to the corresponding absorbance value from day 1 and plotted.

Mouse tumorigenesis assay

All mice were handled in accordance with the guideline of Institutional Animal Care and Use Committee at University of Texas Southwestern under protocol APN 2015-101118. The Alb-Cre; $Lin28a^{f/f}$; $Lin28b^{f/f}$, and $p53^{f/f}$ mice were on the FVB strain background. Our preliminary studies showed that simpler backgrounds such as Alb-Cre;$p53^{f/f}$ developed tumors too readily and masked the oncogenic effects of METTL14 mutations. Liver cancer–inducing oncogenes (pT-CAG/NrasG12V) were coinjected with pT3-$METTL3^{WT}$ and pT3-$METTL14^{WT/R298P/D312A}$ along with Sleeping Beauty Transposase (SB100) using the HDT method into 6-week-old mice. Mice body weights were recorded, and livers were harvested 6 weeks after HDT. Gross livers were weighed and photographed to determine the tumor burden. Mouse livers retrieved from the tail vein injection experiment were fixed in 10% neutral-buffered formalin, dehydrated, cleared, and infiltrated with paraffin according to the standard protocol. Five-micrometer paraffin sections were prepared from the processed organs and stained with hematoxylin and eosin. Images were captured by a bright-field microscope (10× objective) and independently reviewed by a certified pathologist (Evers, B.) affiliated with the UT Southwestern Histopathology Core.

m^6A-seq and data analysis

The procedure was adapted from the original m^6A-seq or Methylated RNA Immuno-precipitation with sequencing (MeRIP-seq) protocols (*10*, *11*). Three biological replicates of 40 million (2 mm–by–150 mm plates) HepG2 cells of stable overexpression of EGFP, $METTL14^{WT}$, $METTL14^{R298P}$, and $METTL14^{D312A}$ were lysed by TRIzol, and the total RNA was extracted. The total RNA was treated by DNase I (5 U per 100 μg total RNA), and mRNAs were enriched by NEBNext Poly(A) mRNA magnetic isolation module (NEB, E7490L). Eight to ten micrograms of mRNA from each sample was fragmented to the size of ~120 nt by Ambion Fragmentation reagent (Thermo Fisher Scientific, AM8740) in a proportional volume (10 μl reaction per 1 μg mRNA) at 70°C for 7 min and then precipitated in 75% ethanol with 10% volume of sodium acetate (3 M, pH 5.5) and GlycoBlue (1 μl, Invitrogen, AM9515). The RNA fragments were dissolved in nuclease-free H_2O at a concentration of 100 ng/μl, and 200 ng from each sample was spared as input. Five micrograms of RNA fragment was denatured and incubated with 15 μg of anti-m^6A antibody (Abcam, ab151230) in immunoprecipitation (IP) buffer [10 mM tris (pH 7.5), 150 mM NaCl, 0.1% NP-40, 5 mM EDTA (pH 8.0), and SUPERase·In (0.2 U/μl] for 4 hours at 4°C. The complex was incubated with 100 μl of slurry of protein A/G beads blocked by bovine serum albumin (0.5 mg/ml in IP buffer) at 4°C overnight. The beads were washed by 0.9 ml, twice of each IP buffer, high-salt buffer [10 mM tris (pH 7.5), 1 M NaCl, 1% NP-40, and 0.5% sodium deoxycholate], low-salt buffer [10 mM tris (pH 7.5), 50 mM NaCl, and 0.1% NP-40], and FastAP buffer [10 mM tris (pH 8.0), 5 mM $MgCl_2$, 100 mM KCl, and 0.02% Triton X-100]. The IP samples were dephosphorylated on-bead by 5 U of FastAP (Thermo Fisher Scientific, EF0615) in 100 μl slurry at 37°C for 30 min in a thermomixer with 15-s pulse shaking at 1200 rpm every 5 min and then washed by FastAP buffer and T4 RNA ligase buffer [50 mM tris (pH 7.5), 10 mM $MgCl_2$, and 1 mM dithiothreitol (DTT)]. A linker RNA oligonucleotides purchased from IDT was pre-adenylated at 5′ -end by T4 RNA ligase I (NEB, 0437) using a method described previously (*43*). The pre-adenylated linker RNA (100 pmol) was added to the 3′ -end of IP RNAs on-bead by 500 U of T4 RNA ligase 2, truncated K227Q (NEB, M0351) in 50 μl of slurry [with a 25% final concentration of polyethylene glycol, molecular weight 800 (PEG 8000)] at 16°C for an overnight incubation in a thermomixer with pulse shaking and then washed by T4 RNA ligase buffer and high-salt buffer. The input samples were dephosphorylated

and ligated to the pre-adenylated linker RNA similarly in tubes, except that the reactions were scaled down 5 times and 2.5 times, respectively. Precipitation of RNA in 80% ethanol was performed after both reactions for the input samples. The IP RNA on-bead was eluted twice by incubation with 100 μg of proteinase K in 100-μl slurry [50 mM tris (pH 8.0), 50 mM NaCl, 1 mM EDTA, 1% SDS, and SUPERase·In (0.4 U/μl)] at 50°C for 1 hour in a thermomixer with pulse shaking, extracted by acid phenol–chloroform, and precipitated in 75% ethanol with GlycoBlue and 0.1× volume of NaCl (2 M). Input and IP RNA were reversed transcribed by RT primer using SuperScript III and the excessive RT primer was removed by ExoSAP-IT. The RNA template in RT reactions was removed by NaOH (3 μl, 1 M) hydrolysis at 70°C for 12 min, and the reaction was neutralized by 3 μl HCl (1 M). The resulting first-strand was cleaned by MyONE Silane beads (Invitrogen, 37002D) before ligated to a single-stranded DNA adaptor fused with 10–random nucleotide Unique Molecular Identifier (UMI) (60 pmol) by T4 RNA ligase 1 (45 U) in a 30-μl reaction with 20% PEG8000, and cleaned again by MyONE Silane beads after ligation. The standard Nextera i5 and i7 barcodes were added to the adapted cDNA by a 13-cycle of PCR amplification. The double-stranded DNAs (dsDNAs) were resolved on 2% agarose gel, and the fragments within the 175 to 250–base pair (bp) range were eluted and pooled for Illumina NextSeq500 single-end 75-bp sequencing with expected sequencing depth of 25 million reads.

The quality of resulting m^{6}A-seq datasets were assessed using the FastQC (version 0.11.2) (http://www.bioinformatics.babraham.ac.uk/projects/fastqc) and FastQ Screen (version 0.4.4) (http://www.bioinformatics.babraham.ac.uk/projects/fastq_screen). The low-quality reads and sequencing adapters were removed by Trim Galore (version 0.4.4) (https://www.bioinformatics.babraham.ac.uk/projects/trim_galore). The reads were aligned to the human reference genome (hg38) using STAR (version 2.7.9a) (*44*), with the parameters set for aligning reads once. The duplicated alignments were eliminated using Picard toolkit (Broad Institute). The resulting primary mapped reads were 6.6 to 22.3 million per sample. Uniquely mapped reads were called peaks for the IP populations against its input by model-based analysis of chromatin immunoprecipitation sequencing (ChIP-seq) (MACS, version 2.1.2) (*45*) with additional parameters (--nomodel --extsize 66 -p 1.00e-05). To achieve a higher resolution and stringency, the resulting summits (coordinates of single nucleotide) from peak-calling were defined as the center of the 50-nucleotide (nt) peaks, which is the default peak-length in this m^{6}A-seq study. The 50-nt peaks overlapped among three replicates (at least 1-nt with at least one other replicate) derived from the same cell line were assembled as intersectional population using HOMER (version 4.9) mergePeaks function (*46*). Each peak summit of newly defined reproducible total populations was the average of three original summit coordinates, which participated in overlap. The peak region of the reproducible total population was expanded to 50-nt around its summit. The peak population unique to each cell line (nonoverlapping with any peak from the other three cell lines) was obtained by another round of HOMER mergePeaks analysis. The resulting peak population numbers were summarized (Fig. 2A). The percentage overlap of total m^{6}A-seq peaks between any two replicates were calculated during the mergePeaks analysis and depicted in a series of heatmaps (fig. S3A) to illustrate the sample pairwise-comparison of the peak-overlapping situation. Metagene plots (fig. S3C) depicting the distribution of m^{6}A sites across the length of mRNA transcripts were generated by MetaPlotR (*47*). For the analysis of site distribution on genomic regions (fig. S3B), the location of peaks was annotated by the annotatePeaks module in HOMER. For the discovery of methylation site sequence consensus of the reproducible total population from each cell line (fig. S3D), the coordinates of 50-nt peaks were analyzed by the findMotifsGenome module in HOMER for a de novo search. For the discovery of methylation site sequence consensus of the unique population from each cell line (Fig. 2B), the strand information of the summits was retrieved from the source of GTF files on Genecode (*48*). The actual 50-nt sequences of the peaks were extracted using BEDtools (version 2.17.0) (*49*) getfasta function with appropriate strand orientation and then analyzed by MEME (version 5.1.1) using the Classic mode. The output position-specific probability matrices from HOMER and MEME analysis were reconstituted to logographs by the Seq2Logo (version 2.0).

For the m^{6}A-seq quantitative analysis, the full union of summits of MACS peak calling from three replicates was designated as the methylation sites index for each cell line. The read count aligned on the methylation site index was converted from the STAR alignment by the bedcov function in Samtools (version 1.10). To compare the methylation levels of R298P versus EGFP on the R298P methylation sites index, the m^{6}A-seq read counts of all three replicates from EGFP and R298P were determined, converted to counts per minute, normalized to input sample Transcripts Per Million (TPM) of the corresponding transcript, and averaged. The ratio and $\log_2$ fold change were calculated and used in the plot (Fig. 2C). The same process was done for the pairwise comparisons of WT versus EGFP and D312A versus EGFP. The methylation sites from each comparison were ranked by $\log_2$ fold change. The 5% sites with the highest and lowest relative m^{6}A enrichment were defined as the population top 5% and bottom 5%, respectively. To describe the methylation consensus sequence of the sites with the highest or the lowest relative m^{6}A enrichment, 50 nt surrounding the summits were extracted and analyzed by MEME.

For the demonstration of representative transcripts harboring the GGAU sites (Fig. 2E and fig. S3G), the aligned sequencing reads files derived from input and IP were visualized by Integrative genomics viewer (version 2.8.0) (*50*) as tracks with a height normalized to count of mapped reads. m^{6}A site enrichment (top track) and input (bottom track) were presented in pairs for each m^{6}A-seq population. The corresponding GGAU sites in transcripts were manually located within 50-nt of the peak region.

Differential RNA expression analysis

Mapped reads from three biological replicates of input RNA samples of each cell line in m^{6}A-seq experiment were counted by featureCounts module of Rsubread package (version 1.4.6) (*51*). ComBat-seq was used for correcting batch effects between libraries prepared and sequenced at different times (*52*). Normalized read counts, TPM, were calculated using RSEM (*53*). Differential RNA expression analysis in pairwise comparisons between cell lines were performed using edgeR (*54*). The transcripts with zero count were eliminated, and the TPM values from three replicates were used to calculate $\log_2$ fold change and FDR. GO analysis was performed using Ingenuity Pathway Analysis tool (Qiagen) and DAVID (*55*).

Proteomics analysis by online 2D LC-MS/MS

Approximately 2×10^6 cells were lysed by incubating in 120 μl of CelLytic M (Sigma-Aldrich, C2978) containing protease inhibitor cocktails on ice for 30 min. The cell lysates were centrifuged at 16,000*g* for 30 min at 4°C to remove cell debris. The proteins were

quantified by using Bradford assay and subsequently subjected to filter-aided sample preparation using trypsin as the digestion enzyme, as described previously (*56*). In brief, 80 μg of total proteins were denatured in a buffer containing with 8 M urea and 50 mM NH_4HCO_3 in a 30-kDa molecular weight cutoff polyethersulfone membrane centrifugal filter unit (VWR, 82031-354). Cysteines in the denatured proteins were reduced and alkylated by incubating with 20 mM DTT at 37°C for 1 hour and 55 mM iodoacetamide in the dark at room temperature for 20 min. The samples were washed three times with 50 mM NH_4HCO_3 to remove urea and excess reagents before being digested with 2 μg of trypsin at 37°C for 18 hours, and the resulting tryptic peptides were desalted with C_{18} tips (Thermo Fisher Scientific, 87784). For tandem mass tags (TMTs) isobaric labeling, 10% of the resulting peptides were reconstituted in 8.5 μl of 50 mM Hepes (pH 8.5). Approximately, 4% of the TMTsixplex reagents (Thermo Fisher Scientific, 90068) were added, and the resulting mixtures were vortexed at room temperature for 2 hours. The reactions were quenched by 0.5% final concentration of hydroxylamine, and the mixture was further vortexed at room temperature for an additional 15 min. To each sample was added 8.92 μl of solution of water/acetonitrile/formic acid (8/1/1, v/v), and the mixture was desalted with C_{18} tips.

Liquid chromatography tandem MS (LC-MS/MS) analysis of TMT-labeled peptides was conducted on an Orbitrap Fusion Lumos tribrid mass spectrometer (Thermo Fisher Scientific) coupled with an Easy-nLC 1200 UPLC system (Thermo Fisher Scientific). The mass spectrometer was equipped with a high-field asymmetric-waveform ion mobility spectrometry (FAIMS), where the compensation voltages (CVs) were set at −40, −60, and −80 V. The carrier gas flow was set at 4.2 liter/min. The cycle time was 3 s with each CV being scanned for 1 s. The online two-dimensional (2D) LC was conducted as described previously (*57*). In brief, desalted peptides were reconstituted in 10 ml of 5 mM ammonium formate/5% acetonitrile and loaded onto a 3-cm capillary strong cation exchange (SCX) column [150-μm inside diameter (ID)] packed in-house with Luna SCX resin (5 μm in particle size and 100 Å in pore size, Phenomenex) with buffer A (0.1% formic acid in water) at a flow rate of 3 ml/min. The peptides were sequentially eluted by a concentration-series of 5-ml plugs of ammonium formate/acetonitrile solutions. The concentration series are (millimolar of ammonium formate/% of acetonitrile) #1, 5/5; #2, 70/5; #3, 100/5; #4, 150/5, #5, 200/5; #6, 500/5; #7, 200/10; #8, 200/15; #9, 200/20; #10, 250/5; #11, 300/5; #12, 350/5; #13, 200/25; #14, 1000/5. The peptides eluted from the SCX column were loaded onto a 3-cm capillary C_{18} column (150-μm ID) packed in-house with C_{18} resin (5 μm in particle size and 120 Å in pore size, Dr. Maisch GmbH HPLC) with buffer A (0.1% formic acid in water) at a flow rate of 3 ml/min. The peptides were eluted from the C_{18} trapping column and separated on a ~25-cm analytical column (5 μm in particle size and 120 Å in pore size, Dr. Maisch GmbH HPLC) packed in-house with C_{18} resin (3 μm in particle size and 120 Å in pore size, Dr. Maisch GmbH HPLC) at a flow rate of 300 nl/min using a linear gradient of 5 to 37% buffer B (80% acetonitrile/0.1% formic acid in water) over 210 min. Eluted peptides were ionized with a Flex nanoelectrospray ion source (Thermo Fisher Scientific). The capillary inlet temperature was set at 305°C, and the spray voltage was set to 2 kV. Full scan in the range of mass/charge ratio 400 to 1500 were acquired at a resolution of 50 k. Maximal injection time and the Automatic Gain Control (AGC) were set as default for full-scan MS. For MS/MS acquisition, precursor ions were isolated at a window of 0.5 Th and subsequently fragmented by higher-energy collisional dissociation at a normalized collisional energy of 38. Fragment ions were scanned at a resolution of 50 k.

Raw LC-MS/MS files were converted to mzXML format and processed in MaxQuant (version 2.0.1.0) (*58*). Methionine oxidation and N-terminal acetylation were set as variable modifications; cysteine carbamidomethylation was specified as a fixed modification. The type of LC-MS run was set to "Reporter ion MS2" with "6plexTMT" as isobaric labels. Reporter ion mass tolerance and the mass tolerance for MS/MS were set at 0.01 Th and 20 parts per million (ppm), respectively. Mass tolerance for full-scan MS was set as 20 and 4.5 ppm for the first and main searches, respectively. Two wmissed cleavages were allowed for trypsin. Peptide spectra were searched against target-decoy UniProt human proteome database (UP000005640), and the proteins were subsequently filtered at 1% false discovery rate. A minimum ratio determined from two peptides was used for protein quantification. The potential contamination and the decoys were removed from the output files. The reporter ion intensities of each protein were normalized against the mean within the samples. The peptide-spectrum match counts derived from the identical protein were aggregated and used as input for differential expression analysis by Limma (*56*). Genes filtered by adj. P value < 0.05 were subjected to pairwise Ingenuity Pathway Analysis where R298P was compared to others.

In vitro methylation sequencing

A degenerate DNA oligonucleotide mixture (table S2) consisting of 20 random-nucleotide (N_{20}) and flanking constant regions was synthesized by MilliporeSigma with manual adjustment to achieve the overall equal ratio of nucleotides. An initial dsDNA library was produced by a seven-cycle PCR amplification in a 1-ml reaction containing 20 pmol of N_{20} oligonucleotides as a template to preserve the designed library complexity. The dsDNA was then gel eluted and transcribed into a randomized RNA library. The RNA library (6.25 μM) was methylated by the target recombinant methyltransferase heterodimer (0.25 μM) in a 20-μl reaction [50 mM tris (pH 7.5), 0.01% Triton X-100, 15 mM NaCl, 1 mM DTT, 1% glycerol, 5 μM SAM (Sigma-Aldrich, A7007), and 20 U SUPERase·In (Invitrogen AM2694)] at room temperature for 2 hours. The methylated RNA library was extracted by acid phenol–chloroform and precipitated with isopropyl alcohol before being reconstituted in nuclease-free water. The purified RNA library was incubated with 7 μg of antibody against m^6A (Abcam, ab151230 or SySy, 202003) in 100 μl of low-salt binding buffer containing 50 mM tris (pH 7.5), 150 mM NaCl, 0.1% NP-40, and 50 U SUPERase·In, and bound to protein A/G beads (Thermo Fisher Scientific, 88802). The mock control sample was prepared by the same procedures but incubated with beads in the absence of antibody. The protein A/G beads were washed with 0.9 ml of low-salt binding buffer once and high-salt buffer [50 mM tris (pH 7.5), 500 mM NaCl, and 0.1% NP-40] twice and then one more time by the low-salt binding buffer before the elution by 0.1 M glycine (pH 2.5). Methylated RNA species were recovered from the elution and reverse transcribed using the RT primer and SuperScript III (Invitrogen, 18080044). Excessive RT primer was digested with ExoSAP-IT (Applied Biosystems, 78250). The resulting cDNA was adapted for barcoding by 10 cycles of PCR amplification, and the dsDNA was purified by PureLink PCR Micro kit (Invitrogen, K310010). The standard Nextera i5 and i7 barcodes were added to the dsDNA by another five cycles of PCR amplification before pooling for Illumina NextSeq500 single-end 75-bp sequencing. The sequencing was performed

at Next Generation Sequencing Core, Eugene McDermott Center, University of Texas Southwestern Medical Center. The 20- and 21-nt constant flanking sequences from the N_{20} oligonucleotides were used to trim the reads by using the Trim Ends module in Geneious (version 2021.2.2). The reads with the length of 20 nt after trimming were selected for motif analysis by MEME (*59*) using the Differential Enrichment mode with the mock control set as background. The output position-specific probability matrices were reconstituted to logograph by the Seq2Logo (version 2.0) (*60*).

Systematic evolution of ligands by exponential enrichment

The experiment was performed similarly as described previously (*27*). An aliquot (0.2 nmol) of randomized RNA library produced for IVM-seq experiment was incubated with equal molarity of 6× His-tag fused target protein complex immobilized on 7 μl of Ni–nitrilotriacetic acid (NTA) magnetic agarose beads (Thermo Fisher Scientific, 78605) in the SELEX-binding buffer [10 mM tris (pH 8.0), 150 mM NaCl, 10 mM $MgCl_2$, 0.01% NP-40, 1% glycerol, 1 mM β-mercaptoethanol, and 10 U SUPERase·In] at 22°C for 30 min on a thermomixer with 15-s pulse shaking at 1200 rpm every 5 min. After being washed for three times by 180 μl of SELEX-binding buffer, the RNA species with affinity was recovered from the beads by heating at 65°C for 5 min in 1 mM tris (pH 7.5) buffer containing 20 pmol of RT primer (same as used in IVM-seq). The elution of RNA was assembled in an RT reaction similarly as in IVM-seq. The subsequent cDNA was amplified by dsDNA amplification primers and 100 μl of PCR reaction to generate the dsDNA template for the next cycle of SELEX. Five SELEX cycles were performed before generating the library for high-throughput sequencing. The SELEX samples were adapted and sequenced together with IVM-seq samples. The sequence data were processed, and motifs analysis was performed identically as for IVM-seq.

In vitro methylation/demethylation assay

Purification of recombinant full-length METTL3-METTL14 protein complexes was carried out as described for the WT (*4*). The RNA oligonucleotides used for methylation activity screen (fig. S1E and Figs. 3, C and D, and 5D) were derived from the context of *MALAT1* methylation site 2577 with single-nucleotide substitutions of the fourth or fifth position within the GGACU site (table S2). The RNA oligonucleotides and substitutions derived from SON, pri-miR-30a, and the linear artificial RNA (Fig. 3E) are also shown in fig. S4C and table S2. The predicted secondary structures were calculated using (*61*). All RNA oligonucleotides were purchased from MilliporeSigma or IDT. The in vitro methylation assay was carried out as previously described (*4*, *29*). Briefly, 100 nM purified methyltransferase complex was mixed with 200 nM RNA oligo and 466 nM *S*-[methyl-^{3}H]-adenosyl-L-methionine (Revvity, NET155H001MC) in IVM buffer [20 mM tris (pH 7.5), 10 mM NaCl, 50 μM $ZnCl_2$, 0.01% Triton X-100, 1% glycerol, 1 mM DTT, and 1 U NxGen ribonuclease inhibitor] and incubated at 22°C for 1 hour. The reactions were blotted onto a membrane that was washed before being counted on a scintillation counter. The amount of tritium incorporation was measured as DPM.

For the in vitro demethylation assay, RNA oligonucleotides (2 μM) containing GGAC or GGAU were methylated by incubating with recombinant METTL3-METTL14^{WT} (2.29 μM) or METTL3-METTL14^{R298P} (2.57 μM) with 5 μM SAM (spiked with 0.35 μM ^{3}H-methyl SAM) at 37°C for 3 hours in IVM buffer. Methylated RNA oligos were purified by Zymo Oligo clean and concentrator kit (Zymo Research, D4060), and the ^{3}H-methyl incorporation was measured by scintillation counting. Purification of recombinant FTO (amino acids 1 to 505) and ALKBH5 (amino acids 69 to 394) was carried out as described in a previous study (*33*). Demethylation was carried out by mixing the eraser at indicated concentrations with 500 nM methylated RNA oligo in the demethylation buffer [25 mM bis-tris (pH 6.5), 50 mM NaCl, 2 mM sodium L-ascorbate, 0.3 mM α-ketoglutaric acid sodium salt, and 0.15 mM ammonium iron(II) sulfate] at 37°C for 30 min (ALKBH5) or 2 hours (FTO). The reactions were quenched by adding 2 mM EDTA. The sampling and measurement procedures are identical to the in vitro methylation assay. To calculate % demethylation, the level of remaining tritium was compared to mock demethylation samples with no added enzyme. All reactions were performed in triplicates, and the statistical tests used are described in the figure legends.

Crystallization and structure refinement

The mutant methyltransferase domain complexes were expressed by introducing the mutation using QuickChange site-directed mutagenesis into the WT methyltransferase domain coexpression construct described in (*4*). Protein purification and crystallization were the same as for the WT. Crystals were grown by using the hanging-drop vapor-diffusion method by mixing 1 μl of protein (15 mg/ml) with 1 μl of reservoir solution containing 0.1 M tris (pH 8.0) and 20% PEG3350 and incubating at 18°C. The datasets were collected at APS-19-ID at wavelength 0.9794 Å. Data were indexed, integrated, and scaled by the program HKL3000 (*62*). Initial phases were obtained by molecular replacement using the WT MTD3/MTD14 complex structure (PDB: 5K7M) as a search model. The model was further built manually with COOT (*63*) and iteratively refined using phenix.refine (*64*). The PROCHECK program was used to check the quality of the final model, which shows good stereochemistry according to the Ramachandran plot (*65*). All structure figures were generated by using the PyMOL (Schrodinger LLC). The software used in this project was curated by SBGrid (*66*).

Electrophoretic mobility shift assay

RNA oligonucleotides derived from MALAT1 (table S2) were labeled at 5′ ends with ^{32}P–adenosine triphosphate using T4 polynucleotide kinase. The recombinant protein purification for METTL3-METTL14 complex, FTO, and ALKBH5 has been described in other sections of Materials and Methods. YTH proteins were overexpressed in Rosetta (DE3) pLysS cells (Novagen) at 18°C and purified using Ni-NTA agarose (Qiagen). Proteins were further purified by ion exchange and size exclusion chromatography. METTL3-METTL14 complexes (concentrations indicated in the legend) were mixed with each RNA (1 nM) in a binding buffer [25 mM tris (pH 8.0), 150 mM NaCl, 1 mM DTT, 5 mM KCl, 10% (v/v) glycerol, 0.01% (vv) Tween-20, 0.01% (v/v) NP-40, 0.01% (v/v) Triton X-100, yeast tRNA (4 ng/μl)] before resolving on 8% native polyacrylamide gels. EMSAs for YTH proteins, FTO, and ALKBH5 were performed similarly except for the binding buffers. The YTH protein EMSAs were carried out in 20 mM bis-tris (pH 7.0), 150 mM NaCl, 5 mM DTT, yeast tRNA (2 ng/μl; 8 ng/μl for YTHDF2 full-length), and 5% (v/v) glycerol; FTO EMSAs were in 20 mM bis-tris (pH 6.5), 53 mM NaCl and 10% (v/v) glycerol; ALKBH5 EMSAs were in 20 mM tris (pH 7.5), 153 mM NaCl, 5% (v/v) glycerol, and yeast tRNA (0.5 ng/μl). The gels were dried and visualized using a phosphor screen and Typhoon FLA 9500 imager (GE Health).

Western blotting

One million cells were washed in Dulbecco's phosphate-buffered saline and lysed in 100 μl of radioimmunoprecipitation assay buffer [50 mM tris (pH 8.0), 150 mM NaCl, 5 mM EDTA (pH 8.0), 1% NP-40, 0.5% sodium deoxycholate, and 0.1% SDS]. The total protein concentration from the lysate was measured by Rapid Gold BCA protein assay kit (Thermo Fisher Scientific, A53225) to normalize the amount of total protein in each sample. Blotted PVDF membranes were blocked with skim milk (5%) in TBS-T [20 mM tris (pH 7.6), 150 mM NaCl, and 0.05% Tween 20] for 1 hour and incubated with primary antibodies [anti-METTL3, Bethyl A301-567A, 1:1,000 (v/v); anti-METTL14, Thermo Fisher Scientific, PA5-58204, 1:1,000 (v/v); anti-ALKBH5, Proteintech 16837-1-AP, 1:2,000 (v/v); horseradish peroxidase (HRP)–conjugated anti–β-Actin, Sigma-Aldrich, A3854, 1:10,000 (v/v)] overnight at 4°C with agitation. Each membrane was then incubated with the appropriate HRP-conjugated secondary antibodies in TBS-T and visualized by using the enhanced chemiluminescence substrate (Bio-Rad 170-5060) and ChemiDoc (Bio-Rad).

Quantitative PCR

Three biological replicates of HepG2 cells of stable overexpression of EGFP, METTL14^{WT}, METTL14^{R298P}, and METTL14^{D312A} were lysed by TRIzol. The total RNA was extracted and treated by DNase I. cDNA was synthesized from 5 μg of total RNA using oligo dT18 primer (5 μM) and SuperScript III (Thermo Fisher Scientific, 18080044). Quantitative PCR was performed using the gene specific primer sets (table S2) on Bio-Rad CFX-384.

Statistics and reproducibility statement

The Western blot of HepG2 stable cell lines and HEC-1-A stable line with transfection were performed more than once with similar results. The determination of the m^{6}A to adenosine ratio of RNAs from HepG2 stable cell lines was carried out for three biological replicates. Significant difference among means of m^{6}A to adenosine ratio in total RNA (fig. S1F) is not found [$P = 0.3133$, ordinary one-way analysis of variance (ANOVA)]. Significant difference among means of m^{6}A to adenosine ratio in poly(A) RNA (fig. S1G) is found ($P < 0.0001$, ordinary one-way ANOVA). The adjusted P values from post hoc Tukey's multiple comparison test are $P = 0.1667$ (EGFP versus WT, not significant), $P = 0.0011$ (WT versus R298P), $P = 0.0076$ (WT versus D312A), and $P = 0.4019$ (R298P versus D312A, not significant). In cell migration and invasion experiments, four or five or seven independent assays were performed at different times. The microscopic images within each figure panel were from the same representative assay. The data plotted for the quantification (Fig. 1, A and B, and fig. S1I) were statistically tested by an ordinary one-way ANOVA test, and the difference among means was found [$P = 0.0008$ (Fig. 1A); $P < 0.0001$ (Fig. 1B); $P = 0.0001$ (fig. S1I)]. The adjusted P values from post hoc Tukey's multiple comparison test in Fig. 1A are $P = 0.0006$ (WT versus R298P), $P = 0.0083$ (R298P versus D312A), $P = 0.2004$ (WT versus D312A, not significant); in Fig. 1B $P < 0.0001$ (WT versus R298P), $P = 0.0001$ (R298P versus D312A), $P = 0.7936$ (WT versus D312A, not significant): in fig. S1I, $P = 0.0369$ (WT versus R298P), $P < 0.0001$ (R298P versus D312A), $P = 0.0298$ (WT versus D312A). The cell proliferation experiment was performed in three biological replicates. In the mice tail injection experiment, the injection of METTL14^{WT} and METTL14^{R298P} constructs were tested in three cohorts (WT, $n = 14$; R298P, $n = 10$ with two deceased on 35 and 38 days after injection), whereas the METTL14^{D312A} construct was tested in two cohorts ($n = 7$) at different times. Data of liver to body ratio were statistically tested by ordinary one-way ANOVA test ($P = 0.0003$). The adjusted P values from post hoc Tukey's multiple comparison test are $P = 0.0005$ (WT versus R298P), $P = 0.0025$ (R298P versus D312A), and $P = 0.9927$ (WT versus D312A, not significant). The liver tumor tissue images presented in Fig. 1F are representatives of two different cohorts. The photomicrographs (Fig. 1E) of histological analysis are the representatives from livers of two mice per treatment. The m^{6}A-seq experiment was performed with three biological replicates at two different times. In the motif analysis of the m^{6}A peaks identified through m^{6}A-seq, the P values of the consensus for total sites (fig. S3D) are 1×10^{-609} (EGFP), 1×10^{-604} (WT), 1×10^{-491} (R298P), and 1×10^{-412} (D312A); for unique sites (Fig. 2B): 2.2×10^{-119} (EGFP), 8.7×10^{-75} (WT), 5.6×10^{-103} (R298P), and 8.8×10^{-21} (D312A); for the top 5% m^{6}A enriched sites (Fig. 2D): 7.4×10^{-81} (WT), 7.7×10^{-349} (R298P), and 1.1×10^{-21} (D312A); for the bottom 5% m^{6}A enriched sites (fig. S3E): 4.9×10^{-80} (WT), 4.0×10^{-174} (R298P), and 8.2×10^{-133} (D312A). The RNA differential expression analysis was performed using three independent replicates derived from m^{6}A-seq input samples. Quantitative PCR was performed using three biological replicates. Each Cp value used to calculate the ΔCp is the average of three technical replicates, and the mean ΔΔCp from three biological replicates is shown. Significant differences among means of normalized ΔΔCp is found from multiple unpaired t tests (Holm-Šídák method). The adjusted P values are (from left to right) 0.000067, 0.003577, 0.022717, 0.014916, 0.010704, 0.014916, 0.022717, 0.008168, 0.016658, 0.005696, 0.000018, and 0.003577 in Fig. 1I; <0.000001, 0.000005, 0.003047, 0.009442, 0.005452, 0.009442, 0.001157, and 0.005290 in Fig. 1J. The high-throughput proteomics MS was performed using three biological replicates in different times. The IVM-seq experiment for the identification of methylation site consensus sequence of METTL14^{WT} and METTL14^{R298P} was repeated by using different anti-m^{6}A antibodies. The P value of the consensus logographs generated by MEME analysis are 5.2×10^{-412} (WT, SySy), $1.5 \times 10^{-32,269}$ (WT, Abcam), 4.0×10^{-355} (R298P, SySy), and $9.1 \times 10^{-45,993}$ (R298P, Abcam). The IVM-seq for METTL14^{R298C}, METTL14^{R298H}, and METTL14^{D312A} was performed by using only the SySy anti-m^{6}A antibody. The P values of the consensus logographs are 6.5×10^{-1771} (R298C), 6.9×10^{-1094} (R298H), and 4.6×10^{-7} (D312A). The in vitro methylation assays reported in this study were all carried out in triplicate reactions at the same time. The same assay has been performed by different people more than three times with similar results. The data from the comparison of methylation activity with GGAC and GGAU sites has been statistically tested by an unpaired two-tailed t test. The P values in Fig. 3D are (from left to right) $P = 0.000131$, $P = 0.000867$, $P = 0.000080$, $P = 0.000045$, $P = 0.002601$, $P = 0.000095$, and $P = 0.001398$. The P values in Fig. 5D are (from left to right) $P = 0.000023$, $P = 0.000013$, $P < 0.000001$, $P = 0.763026$, and $P = 0.095956$ (buffer control). The in vitro demethylation assays reported in this study were all carried out in triplicate reactions at the same time. The assay using substrates from different preparations has been performed at least three times with similar results. The data from the comparison of demethylation activity with GG(m^{6}A)CU and GG(m^{6}A)UU sites has been statistically tested by multiple unpaired two-tailed t test (Holm- Šídák method). The adjusted P values in Fig. 4C are (from left to right) $P > 0.999999$ (mock control), $P = 0.689126$, $P = 0.424246$, $P = 0.988989$, and $P = 0.174646$. The adjusted P values in Fig. 4D are (from left to right) $P > 0.999999$

(mock control), $P = 0.022468$, $P = 0.006094$, $P = 0.006094$, and $P = 0.001574$. The EMSA experiments were performed more than three times with similar results. In the SELEX experiment performed to determine the METTL3-METTL14 binding preference, the P values of the top consensus logographs generated by MEME analysis are 3.7×10^{-1045}, 1.5×10^{-894}, and 1.3×10^{-8826} (WT); 2.0×10^{-899}, 1.1×10^{-5651}, and 2.5×10^{-10385} (R298P). For the RNA level comparison of METTL14, METTL3, and ALKBH5 using the RNA-seq data ($n = 3$) from HepG2 OE cell lines, unpaired two-tailed t test was performed. The P values in fig. S1D for METTL14 are $P = 0.0017$ (EGFP versus WT), $P = 0.8208$ (WT versus R298P), $P = 0.9339$ (R298P versus D312A), $P = 0.0045$ (EGFP versus R298P), $P = 0.0001$ (EGFP versus D312A), and $P = 0.6619$ (WT versus D312A). The P values in fig. S1D for METTL3 are $P = 0.7882$ (EGFP versus WT), $P = 0.5855$ (WT versus R298P), $P = 0.9711$ (R298P versus D312A), $P = 0.5097$ (EGFP versus R298P), $P = 0.3949$ (EGFP versus D312A), and $P = 0.4575$ (WT versus D312A). The P values in fig. S5E are $P = 0.2160$ (EGFP versus WT), $P = 0.6122$ (WT versus R298P), $P = 0.6967$ (R298P versus D312A), $P = 0.1857$ (EGFP versus R298P), $P = 0.1673$ (EGFP versus D312A), and $P = 0.8278$ (WT versus D312A).

Supplementary Materials

This PDF file includes:

Figs. S1 to S6
Tables S1 and S2

REFERENCES AND NOTES

1. H. Shi, J. Wei, C. He, Where, when, and how: Context-dependent functions of RNA methylation writers, readers, and erasers. *Mol. Cell* **74**, 640–650 (2019).
2. S. Zaccara, R. J. Ries, S. R. Jaffrey, Reading, writing and erasing mRNA methylation. *Nat. Rev. Mol. Cell Biol.* **20**, 608–624 (2019).
3. J. Liu, Y. Yue, D. Han, X. Wang, Y. Fu, L. Zhang, G. Jia, M. Yu, Z. Lu, X. Deng, Q. Dai, W. Chen, C. He, A METTL3-METTL14 complex mediates mammalian nuclear RNA N6-adenosine methylation. *Nat. Chem. Biol.* **10**, 93–95 (2014).
4. P. Wang, K. A. Doxtader, Y. Nam, Structural basis for cooperative function of Mettl3 and Mettl14 methyltransferases. *Mol. Cell* **63**, 306–317 (2016).
5. X. Wang, J. Feng, Y. Xue, Z. Guan, D. Zhang, Z. Liu, Z. Gong, Q. Wang, J. Huang, C. Tang, T. Zou, P. Yin, Structural basis of N^6-adenosine methylation by the METTL3-METTL14 complex. *Nature* **534**, 575–578 (2016).
6. Y. Wang, Y. Li, J. I. Toth, M. D. Petroski, Z. Zhang, J. C. Zhao, N^6-methyladenosine modification destabilizes developmental regulators in embryonic stem cells. *Nat. Cell Biol.* **16**, 191–198 (2014).
7. J. Liu, M. A. Eckert, B. T. Harada, S. M. Liu, Z. Lu, K. Yu, S. M. Tienda, A. Chryplewicz, A. C. Zhu, Y. Yang, J. T. Huang, S. M. Chen, Z. G. Xu, X. H. Leng, X. C. Yu, J. Cao, Z. Zhang, J. Liu, E. Lengyel, C. He, m^{6}A mRNA methylation regulates AKT activity to promote the proliferation and tumorigenicity of endometrial cancer. *Nat. Cell Biol.* **20**, 1074–1083 (2018).
8. Z. Zhou, J. Lv, H. Yu, J. Han, X. Yang, D. Feng, Q. Wu, B. Yuan, Q. Lu, H. Yang, Mechanism of RNA modification N6-methyladenosine in human cancer. *Mol. Cancer* **19**, 104 (2020).
9. X. Deng, R. Su, X. Feng, M. Wei, J. Chen, Role of N^6-methyladenosine modification in cancer. *Curr. Opin. Genet. Dev.* **48**, 1–7 (2018).
10. D. Dominissini, S. Moshitch-Moshkovitz, S. Schwartz, M. Salmon-Divon, L. Ungar, S. Osenberg, K. Cesarkas, J. Jacob-Hirsch, N. Amariglio, M. Kupiec, R. Sorek, G. Rechavi, Topology of the human and mouse m^{6}A RNA methylomes revealed by m^{6}A-seq. *Nature* **485**, 201–206 (2012).
11. K. D. Meyer, Y. Saletore, P. Zumbo, O. Elemento, C. E. Mason, S. R. Jaffrey, Comprehensive analysis of mRNA methylation reveals enrichment in 3′ UTRs and near stop codons. *Cell* **149**, 1635–1646 (2012).
12. C. M. Wei, A. Gershowitz, B. Moss, 5′-Terminal and internal methylated nucleotide sequences in HeLa cell mRNA. *Biochemistry* **15**, 397–401 (1976).
13. C. M. Wei, B. Moss, Nucleotide sequences at the N^6-methyladenosine sites of HeLa cell messenger ribonucleic acid. *Biochemistry* **16**, 1672–1676 (1977).
14. S. A. Forbes, D. Beare, P. Gunasekaran, K. Leung, N. Bindal, H. Boutselakis, M. Ding, S. Bamford, C. Cole, S. Ward, C. Y. Kok, M. Jia, T. De, J. W. Teague, M. R. Stratton, U. McDermott, P. J. Campbell, COSMIC: Exploring the world's knowledge of somatic mutations in human cancer. *Nucleic Acids Res.* **43**, D805–D811 (2015).
15. K. Miyake, P. H. Costa Cruz, I. Nagatomo, Y. Kato, D. Motooka, S. Satoh, Y. Adachi, Y. Takeda, Y. Kawahara, A. Kumanogoh, A cancer-associated METTL14 mutation induces aberrant m6A modification, affecting tumor growth. *Cell Rep.* **42**, 112688 (2023).
16. B. Linder, A. V. Grozhik, A. O. Olarerin-George, C. Meydan, C. E. Mason, S. R. Jaffrey, Single-nucleotide-resolution mapping of m6A and m6Am throughout the transcriptome. *Nat. Methods* **12**, 767–772 (2015).
17. K. D. Meyer, DART-seq: An antibody-free method for global m^{6}A detection. *Nat. Methods* **16**, 1275–1280 (2019).
18. Z. Zhang, L. Q. Chen, Y. L. Zhao, C. G. Yang, I. A. Roundtree, Z. Zhang, J. Ren, W. Xie, C. He, G. Z. Luo, Single-base mapping of m^{6}A by an antibody-independent method. *Sci. Adv.* **5**, eaax0250 (2019).
19. P. Sledz, M. Jinek, Structural insights into the molecular mechanism of the m^{6}A writer complex. *eLife* **5**, e18434 (2016).
20. A. B. R. McIntyre, N. S. Gokhale, L. Cerchietti, S. R. Jaffrey, S. M. Horner, C. E. Mason, Limits in the detection of m^{6}A changes using MeRIP/m^{6}A-seq. *Sci. Rep.* **10**, 6590 (2020).
21. X. L. Ping, B. F. Sun, L. Wang, W. Xiao, X. Yang, W. J. Wang, S. Adhikari, Y. Shi, Y. Lv, Y. S. Chen, X. Zhao, A. Li, Y. Yang, U. Dahal, X. M. Lou, X. Liu, J. Huang, W. P. Yuan, X. F. Zhu, T. Cheng, Y. L. Zhao, X. Wang, J. M. Rendtlew Danielsen, F. Liu, Y. G. Yang, Mammalian WTAP is a regulatory subunit of the RNA N6-methyladenosine methyltransferase. *Cell Res.* **24**, 177–189 (2014).
22. S. Schwartz, M. R. Mumbach, M. Jovanovic, T. Wang, K. Maciag, G. G. Bushkin, P. Mertins, D. Ter-Ovanesyan, N. Habib, D. Cacchiarelli, N. E. Sanjana, E. Freinkman, M. E. Pacold, R. Satija, T. S. Mikkelsen, N. Hacohen, F. Zhang, S. A. Carr, E. S. Lander, A. Regev, Perturbation of m6A writers reveals two distinct classes of mRNA methylation at internal and 5′ sites. *Cell Rep.* **8**, 284–296 (2014).
23. D. P. Patil, C. K. Chen, B. F. Pickering, A. Chow, C. Jackson, M. Guttman, S. R. Jaffrey, m(6)A RNA methylation promotes XIST-mediated transcriptional repression. *Nature* **537**, 369–373 (2016).
24. P. Knuckles, T. Lence, I. U. Haussmann, D. Jacob, N. Kreim, S. H. Carl, I. Masiello, T. Hares, R. Villasenor, D. Hess, M. A. Andrade-Navarro, M. Biggiogera, M. Helm, M. Soller, M. Bühler, J. Y. Roignant, Zc3h13/Flacc is required for adenosine methylation by bridging the mRNA-binding factor Rbm15/Spenito to the m^{6}A machinery component Wtap/Fl(2)d. *Genes Dev.* **32**, 415–429 (2018).
25. J. Wen, R. Lv, H. Ma, H. Shen, C. He, J. Wang, F. Jiao, H. Liu, P. Yang, L. Tan, F. Lan, Y. G. Shi, C. He, Y. Shi, J. Diao, Zc3h13 regulates nuclear RNA m^{6}A methylation and mouse embryonic stem cell self-renewal. *Mol. Cell* **69**, 1028–1038.e6 (2018).
26. K. Ruzicka, M. Zhang, A. Campilho, Z. Bodi, M. Kashif, M. Saleh, D. Eeckhout, S. El-Showk, H. Li, S. Zhong, G. De Jaeger, N. P. Mongan, J. Hejatko, Y. Helariutta, R. G. Fray, Identification of factors required for m^6 A mRNA methylation in Arabidopsis reveals a role for the conserved E3 ubiquitin ligase HAKAI. *New Phytol.* **215**, 157–172 (2017).
27. C. Tuerk, L. Gold, Systematic evolution of ligands by exponential enrichment: RNA ligands to bacteriophage T4 DNA polymerase. *Science* **249**, 505–510 (1990).
28. N. Liu, M. Parisien, Q. Dai, G. Zheng, C. He, T. Pan, Probing N^6-methyladenosine RNA modification status at single nucleotide resolution in mRNA and long noncoding RNA. *RNA* **19**, 1848–1856 (2013).
29. K. A. Doxtader, P. Wang, A. M. Scarborough, D. Seo, N. K. Conrad, Y. Nam, Structural basis for regulation of METTL16, an S-adenosylmethionine homeostasis factor. *Mol. Cell* **71**, 1001–1011.e4 (2018).
30. C. Xu, X. Wang, K. Liu, I. A. Roundtree, W. Tempel, Y. Li, Z. Lu, C. He, J. Min, Structural basis for selective binding of m6A RNA by the YTHDC1 YTH domain. *Nat. Chem. Biol.* **10**, 927–929 (2014).
31. G. Jia, Y. Fu, X. Zhao, Q. Dai, G. Zheng, Y. Yang, C. Yi, T. Lindahl, T. Pan, Y. G. Yang, C. He, *N*6-methyladenosine in nuclear RNA is a major substrate of the obesity-associated FTO. *Nat. Chem. Biol.* **7**, 885–887 (2011).
32. G. Zheng, J. A. Dahl, Y. Niu, P. Fedorcsak, C. M. Huang, C. J. Li, C. B. Vagbo, Y. Shi, W. L. Wang, S. H. Song, Z. Lu, R. P. Bosmans, Q. Dai, Y. J. Hao, X. Yang, W. M. Zhao, W. M. Tong, X. J. Wang, F. Bogdan, K. Furu, Y. Fu, G. Jia, X. Zhao, J. Liu, H. E. Krokan, A. Klungland, Y. G. Yang, C. He, ALKBH5 is a mammalian RNA demethylase that impacts RNA metabolism and mouse fertility. *Mol. Cell* **49**, 18–29 (2013).
33. S. Kaur, N. Y. Tam, M. A. McDonough, C. J. Schofield, W. S. Aik, Mechanisms of substrate recognition and N6-methyladenosine demethylation revealed by crystal structures of ALKBH5-RNA complexes. *Nucleic Acids Res.* **50**, 4148–4160 (2022).
34. C. Tang, R. Klukovich, H. Peng, Z. Wang, T. Yu, Y. Zhang, H. Zheng, A. Klungland, W. Yan, ALKBH5-dependent m6A demethylation controls splicing and stability of long 3′-UTR mRNAs in male germ cells. *Proc. Natl. Acad. Sci. U.S.A.* **115**, E325–E333 (2018).
35. Y. L. Xiao, S. Liu, R. Ge, Y. Wu, C. He, M. Chen, W. Tang, Transcriptome-wide profiling and quantification of N^6-methyladenosine by enzyme-assisted adenosine deamination. *Nat. Biotechnol.* **41**, 993–1003 (2023).

36. C. Liu, H. Sun, Y. Yi, W. Shen, K. Li, Y. Xiao, F. Li, Y. Li, Y. Hou, B. Lu, W. Liu, H. Meng, J. Peng, C. Yi, J. Wang, Absolute quantification of single-base m^{6}A methylation in the mammalian transcriptome using GLORI. *Nat. Biotechnol.* **41**, 355–366 (2023).
37. L. Dang, D. W. White, S. Gross, B. D. Bennett, M. A. Bittinger, E. M. Driggers, V. R. Fantin, H. G. Jang, S. Jin, M. C. Keenan, K. M. Marks, R. M. Prins, P. S. Ward, K. E. Yen, L. M. Liau, J. D. Rabinowitz, L. C. Cantley, C. B. Thompson, M. G. Vander Heiden, S. M. Su, Cancer-associated IDH1 mutations produce 2-hydroxyglutarate. *Nature* **462**, 739–744 (2009).
38. C. Kadoch, D. C. Hargreaves, C. Hodges, L. Elias, L. Ho, J. Ranish, G. R. Crabtree, Proteomic and bioinformatic analysis of mammalian SWI/SNF complexes identifies extensive roles in human malignancy. *Nat. Genet.* **45**, 592–601 (2013).
39. M. Oren, V. Rotter, Mutant p53 gain-of-function in cancer. *Cold Spring Harb. Perspect. Biol.* **2**, a001107 (2010).
40. Y. Sancak, T. R. Peterson, Y. D. Shaul, R. A. Lindquist, C. C. Thoreen, L. Bar-Peled, D. M. Sabatini, The Rag GTPases bind raptor and mediate amino acid signaling to mTORC1. *Science* **320**, 1496–1501 (2008).
41. S. B. Frank, V. V. Schulz, C. K. Miranti, A streamlined method for the design and cloning of shRNAs into an optimized Dox-inducible lentiviral vector. *BMC Biotechnol.* **17**, 24 (2017).
42. C. A. Schneider, W. S. Rasband, K. W. Eliceiri, NIH Image to ImageJ: 25 years of image analysis. *Nat. Methods* **9**, 671–675 (2012).
43. Y. Song, K. J. Liu, T. H. Wang, Efficient synthesis of stably adenylated DNA and RNA adapters for microRNA capture using T4 RNA ligase 1. *Sci. Rep.* **5**, 15620 (2015).
44. A. Dobin, C. A. Davis, F. Schlesinger, J. Drenkow, C. Zaleski, S. Jha, P. Batut, M. Chaisson, T. R. Gingeras, STAR: Ultrafast universal RNA-seq aligner. *Bioinformatics* **29**, 15–21 (2013).
45. Y. Zhang, T. Liu, C. A. Meyer, J. Eeckhoute, D. S. Johnson, B. E. Bernstein, C. Nusbaum, R. M. Myers, M. Brown, W. Li, X. S. Liu, Model-based analysis of ChIP-Seq (MACS). *Genome Biol.* **9**, R137 (2008).
46. S. Heinz, C. Benner, N. Spann, E. Bertolino, Y. C. Lin, P. Laslo, J. X. Cheng, C. Murre, H. Singh, C. K. Glass, Simple combinations of lineage-determining transcription factors prime cis-regulatory elements required for macrophage and B cell identities. *Mol. Cell* **38**, 576–589 (2010).
47. A. O. Olarerin-George, S. R. Jaffrey, MetaPlotR: A Perl/R pipeline for plotting metagenes of nucleotide modifications and other transcriptomic sites. *Bioinformatics* **33**, 1563–1564 (2017).
48. A. Frankish, M. Diekhans, A. M. Ferreira, R. Johnson, I. Jungreis, J. Loveland, J. M. Mudge, C. Sisu, J. Wright, J. Armstrong, I. Barnes, A. Berry, A. Bignell, S. Carbonell Sala, J. Chrast, F. Cunningham, T. Di Domenico, S. Donaldson, I. T. Fiddes, C. Garcia Giron, J. M. Gonzalez, T. Grego, M. Hardy, T. Hourlier, T. Hunt, O. G. Izuogu, J. Lagarde, F. J. Martin, L. Martinez, S. Mohanan, P. Muir, F. C. P. Navarro, A. Parker, B. Pei, F. Pozo, M. Ruffier, B. M. Schmitt, E. Stapleton, M. M. Suner, I. Sycheva, B. Uszczynska-Ratajczak, J. Xu, A. Yates, D. Zerbino, Y. Zhang, B. Aken, J. S. Choudhary, M. Gerstein, R. Guigo, T. J. P. Hubbard, M. Kellis, B. Paten, A. Reymond, M. L. Tress, P. Flicek, GENCODE reference annotation for the human and mouse genomes. *Nucleic Acids Res.* **47**, D766–D773 (2019).
49. A. R. Quinlan, I. M. Hall, BEDTools: A flexible suite of utilities for comparing genomic features. *Bioinformatics* **26**, 841–842 (2010).
50. J. T. Robinson, H. Thorvaldsdottir, W. Winckler, M. Guttman, E. S. Lander, G. Getz, J. P. Mesirov, Integrative genomics viewer. *Nat. Biotechnol.* **29**, 24–26 (2011).
51. Y. Liao, G. K. Smyth, W. Shi, featureCounts: An efficient general purpose program for assigning sequence reads to genomic features. *Bioinformatics* **30**, 923–930 (2014).
52. Y. Zhang, G. Parmigiani, W. E. Johnson, ComBat-seq: Batch effect adjustment for RNA-seq count data. *NAR Genom. Bioinform.* **2**, lqaa078 (2020).
53. B. Li, C. N. Dewey, RSEM: Accurate transcript quantification from RNA-Seq data with or without a reference genome. *BMC Bioinformatics* **12**, 323 (2011).
54. M. D. Robinson, D. J. McCarthy, G. K. Smyth, edgeR: A bioconductor package for differential expression analysis of digital gene expression data. *Bioinformatics* **26**, 139–140 (2010).
55. D. W. Huang, B. T. Sherman, R. A. Lempicki, Systematic and integrative analysis of large gene lists using DAVID bioinformatics resources. *Nat. Protoc.* **4**, 44–57 (2009).
56. G. K. Smyth, Linear models and empirical bayes methods for assessing differential expression in microarray experiments. *Stat. Appl. Genet. Mol. Biol.* **3**, Article3 (2004).
57. H. Liu, J. W. Finch, J. A. Luongo, G. Z. Li, J. C. Gebler, Development of an online two-dimensional nano-scale liquid chromatography/mass spectrometry method for improved chromatographic performance and hydrophobic peptide recovery. *J. Chromatogr. A* **1135**, 43–51 (2006).
58. S. Tyanova, T. Temu, J. Cox, The MaxQuant computational platform for mass spectrometry-based shotgun proteomics. *Nat. Protoc.* **11**, 2301–2319 (2016).
59. T. L. Bailey, M. Boden, F. A. Buske, M. Frith, C. E. Grant, L. Clementi, J. Ren, W. W. Li, W. S. Noble, MEME SUITE: Tools for motif discovery and searching. *Nucleic Acids Res.* **37**, W202–W208 (2009).
60. M. C. Thomsen, M. Nielsen, Seq2Logo: A method for construction and visualization of amino acid binding motifs and sequence profiles including sequence weighting, pseudo counts and two-sided representation of amino acid enrichment and depletion. *Nucleic Acids Res.* **40**, W281–W287 (2012).
61. D. H. Mathews, M. D. Disney, J. L. Childs, S. J. Schroeder, M. Zuker, D. H. Turner, Incorporating chemical modification constraints into a dynamic programming algorithm for prediction of RNA secondary structure. *Proc. Natl. Acad. Sci. U.S.A.* **101**, 7287–7292 (2004).
62. W. Minor, M. Cymborowski, Z. Otwinowski, M. Chruszcz, HKL-3000: The integration of data reduction and structure solution – from diffraction images to an initial model in minutes. *Acta Crystallogr. D Biol. Crystallogr.* **62**, 859–866 (2006).
63. P. Emsley, K. Cowtan, Coot: Model-building tools for molecular graphics. *Acta Crystallogr. D Biol. Crystallogr.* **60**, 2126–2132 (2004).
64. D. Liebschner, P. V. Afonine, M. L. Baker, G. Bunkoczi, V. B. Chen, T. I. Croll, B. Hintze, L. W. Hung, S. Jain, A. J. McCoy, N. W. Moriarty, R. D. Oeffner, B. K. Poon, M. G. Prisant, R. J. Read, J. S. Richardson, D. C. Richardson, M. D. Sammito, O. V. Sobolev, D. H. Stockwell, T. C. Terwilliger, A. G. Urzhumtsev, L. L. Videau, C. J. Williams, P. D. Adams, Macromolecular structure determination using x-rays, neutrons and electrons: Recent developments in Phenix. *Acta Crystallogr. D Struct. Biol.* **75**, 861–877 (2019).
65. R. A. Laskowski, M. W. Macarthur, D. S. Moss, J. M. Thornton, Procheck - A program to check the stereochemical quality of protein structures. *J. Appl. Cryst.* **26**, 283–291 (1993).
66. A. Morin, B. Eisenbraun, J. Key, P. C. Sanschagrin, M. A. Timony, M. Ottaviano, P. Sliz, Collaboration gets the most out of software. *eLife* **2**, e01456 (2013).

Acknowledgments: We thank O. Koczy, J. Parker, and R. Setlem for contributing to preliminary studies. We are grateful for the helpful discussions with B. Xhemalce on genomic data analysis. The Structural Biology Laboratory at UT Southwestern for help with synchrotron data collection. The use of the SBC 19ID beamline at Advanced Photon Source is supported by the US Department of Energy contract DE-AC02-06CH11357. We thank M. McCoy and B. Posner in the High-throughput Screening Core at UT Southwestern for help with mass spectrometry experiments. All deep sequencing data were obtained through the Next Generation Sequencing Core at the McDermott Center for Human Growth and Development at UT Southwestern. pLJM1-EGFP plasmid was a gift from D. Sabatini. pEZ-Tet-pLKO-Puro was a gift from C. Miranti. pMD2.G and psPAX2 were gifts from D. Trono. **Funding:** This work was supported by NIH/NIGMS (R01GM122960 to Y.N.), NIH/NCI (R01CA258589 to Y.N.), NIH/NIEHS (R35ES031707 to Y.W.), Cancer Prevention Research Institute of Texas (RP190259 to Y.N.), and Welch Foundation (I-2115-20220331 to Y.N.). R.L.S. is a McKnight Fellow. Y.N. is a Southwestern Medical Foundation Scholar in Biomedical Research, UT Southwestern Presidential Scholar, Doris and Bryan Wildenthal Distinguished Chair in Medical Science, a Pew Biomedical Scholar, and a Packard Fellow for Science and Engineering. **Author contributions:** Conceptualization: Y.N., C.Z., and H.Z. Methodology: C.Z., Y.N., Y.-Y.Y., L.T., H.Z., Y.W., and M.-H.H. Software: C.X. Validation: C.Z., Y.N., L.T., E.H., B.B.K., Y.W., K.A.D.L., R.L.S., and M.-H.H. Formal analysis: C.Z., Y.N., A.K., C.X., Y.-Y.Y., L.T., B.B.K., Y.W., X.Z., and M.-H.H. Investigation: C.Z., Y.N., Y.-Y.Y., B.E., L.T., E.H., B.B.K., P.W., Y.W., K.A.D.L., R.L.S., and M.-H.H. Resources: C.Z., Y.N., Y.-Y.Y., E.H., H.Z., and M.-H.H. Data curation: C.Z., C.X., and M.-H.H. Writing—original draft: C.Z. and Y.N. Writing—review and editing: C.Z., Y.N., C.X., P.W., H.Z., Y.W., and K.A.D.L. Visualization: C.Z., Y.N., B.E., L.T., and M.-H.H. Supervision: Y.N., C.X., and Y.W. Project administration: Y.N., C.X., Y.W., and M.-H.H. Funding acquisition: Y.N. and Y.W. **Competing interests:** H.Z. is a cofounder of Quotient Therapeutics and Jumble Therapeutics and is an advisor for Newlimit, Alnylam Pharmaceuticals, and Chroma Medicines. H.Z. receives research support from Chroma Medicines and owns stock in Ionis and Madrigal Pharmaceuticals. The authors declare that they have no other competing interests. **Data and materials availability:** The reagents generated in this study can be provided by Y.N. pending scientific review and a completed material transfer agreement. Requests for the reagents should be submitted to: yunsun.nam@utsouthwestern.edu. The atomic coordinates and the structure factors have been deposited in the Protein Data Bank under accession numbers 7RX7, 7RX8, and 7RX6, for structures of the methyltransferase domains of METTL3-METTL14^{R298P}, METTL3-METTL14^{R298H}, and METTL3-METTL14^{R298C}, respectively. The m^{6}A-seq data have been deposited to the Gene Expression Omnibus database (GSE192859), IVM-seq, and SELEX data to Dryad (doi:10.5061/dryad.37pvmcvvb), and proteomics data to proteomeXchange (PXD039447). All data needed to evaluate the conclusions in the paper are present in the paper and/or the Supplementary Materials.

Submitted 14 August 2024
Accepted 14 November 2024
Published 20 December 2024
10.1126/sciadv.ads4750